2005

Integrating visible, near infrared and short wave infrared hyperspectral and multispectral thermal imagery for geological mapping at Cuprite, Nevada

Xianfeng Chen
West Virginia University

Integrating visible, near infrared and short wave infrared hyperspectral and multispectral thermal imagery for geological mapping at Cuprite, Nevada

Xianfeng Chen

Dissertation submitted to the
College of Arts and Sciences
at West Virginia University
in partial fulfillment of the requirements
for the degree of

Doctor of Philosophy
In
Geology

Timothy A. Warner, Ph.D. Chair
David Campagna, Ph.D.
J. Steven Kite, Ph.D.
M. Duane Nellis, Ph.D.
Thomas Wilson, Ph.D.

Department of Geology and Geography

Morgantown, West Virginia
2005

Keywords: Hyperspectral, multispectral thermal infrared, classification, geological mapping, hydrothermal alteration

ABSTRACT

Integrating visible, near infrared and short wave infrared hyperspectral and multispectral thermal imagery for geological mapping at Cuprite, Nevada

Xianfeng Chen

Visible, near infrared (VNIR), and short wave infrared (SWIR) hyperspectral and thermal infrared (TIR) multispectral remote sensing have become potential tool for geological mapping. In this dissertation, a series of studies were carried out to investigate the potential impact of combining VNIR/SWIR hyperspectral and TIR multispectral data for surface geological mapping. First, a series of simulated data sets based on the characteristics of hyperspectral AVIRIS and multispectral TIR MASTER sensors was created from surface reflectance and emissivity library spectra. Five common used classification methods including minimum distance, maximum likelihood, spectral angle mapper (SAM), spectral feature fitting (SFF), and binary encoding were applied to these simulated data sets to test the hypothesis. It was found that most methods applied to the combined data actually obtained improvement in overall accuracy of classification by comparison of the results to the simulated AVIRIS data or TIR MASTER alone. And some minerals and rocks with strong spectral features got a marked increase in classification accuracy. Second, two real data sets such as AVIRIS and MASTER of Cuprite, Nevada were used. Four classification methods were each applied to AVIRIS, MASTER, and a combined set. The results of these classifications confirmed most findings from the simulated data analyses. Most silicate bearing rocks achieved great improvement in classification accuracy with the combined data. SFF applied to the combination of AVIRIS with MASTER TIR data are especially valuable for identification of silicified alteration and quartzite sandstone which exhibit strong distinctive absorption features in the TIR region. SAM showed some advantages over SFF in dealing with multiple broad band TIR data, obtaining higher accuracy in discriminating low albedo volcanic rocks and limestone which do not have strong characteristic absorption features in the TIR region. One of the main objectives of these studies is to develop a automate classification algorithm which is effective for the analysis of VNIR/SWIR hyperspectral and TIR multispectral data. A rule based system was constructed to draw the strengths of disparate wavelength regions and different algorithms for geological mapping.

ACKNOWLEDGEMENTS

I would like to thank all my committee members. I am really grateful for their precious time and efforts offered to me. In particular, I would like to thanks my advisor, mentor, Dr. Tim Warner who has not only invested tremendous time and efforts in my dissertation, but also showed me considerable cares for all aspects.

I am grateful to numerous individuals who supplied me with helps in my dissertation research. For this, I am grateful to Randy Crowe who helped me solve a lot of computer problems. I am indebted to Dr. David Campagna. Under his guiding, we collected field samples and examined lithologic units of Cuprite, Nevada. I would like to thank Dr. S. J. Hook and Ron Alley for providing me with an atmospheric profile acquired at the time of over-flight, and Cindy Grove of the Jet Propulsion Laboratory for measuring the spectra of field collected samples.

I am grateful to my friends, Linda and Art Jacknowitz. Their hospitalities and cares have made us to get use of the new life in Morgantown with ease. I am also grateful to my wife, Hong Zhang who sacrificed her own career to stay at home taking care my daughter and me so that I could focus on my study and research. Finally, I would like to thank all faculties, staff, and graduate students in the department of geology and geography who have help me over the past five years.

This study is supported by West Virginia View.

TABLE OF CONTENTS

LIST FIGURES

LIST OF TABLES

Chapter 1. General Introduction

Visible (0.4 to 0.7 μm), near infrared (0.7-1.1 μm, NIR, also sometimes combined with visible wavelengths as VNIR), and short wave infrared (1.1-2.5 μm, SWIR) hyperspectral remote sensing and thermal infrared (8-12 μm, TIR) multispectral remote sensing technologies have been important tools for geological mapping in arid and semiarid regions for more than 20 years (Crósta *et al.,* 1998; Kruse, 1988; Kruse *et al.,* 1993b; Collins, 1991; Hook *et al*., 1994; Rowan and Mars, 2003; Sabine *et al*., 1994). Hyperspectral imaging refers to the acquisition of images with hundreds or more contiguous spectral bands, which cover a sufficiently narrow region to discriminate spectral features in minerals and other surface materials. Multispectral imaging implies a smaller number of bands, usually in the range of three to ten or more, each of which covers a relatively broad spectral region. The development of hyperspectral VNIR/SWIR and multispectral TIR technologies culminated in the recent launches of the satellite borne Hyperion hyperspectral and ASTER (Advanced Spaceborne Thermal Emission and Reflectance Radiometer) TIR instruments. The advent of satellite acquisitions is important, because when space platforms are used, data is potentially available globally, and on a relatively routine basis. The planned operation of the European sensor, ARES, which has both hyperspectral data and multispectral TIR data, should make the availability of such data routine in geological applications (Mueller *et al*., 2003)

Part of the significance of VNIR/SWIR hyperspectral and TIR multispectral imaging is that these technologies supply information on inherent physical properties, namely reflectance and emissivity, which in turn can be related to rock composition. This link can in theory be made because minerals tend to have characteristic spectral

reflectance and emissivity features (Clark, 1999; Hook *et al*., 1994) that are produced by electronic transitions and vibrational processes resulting from the interaction of electromagnetic energy with atoms and molecules.

Electronic transitions are a result of the change of energy states following the absorption of a photon, and include crystal field effects, charge transfer absorptions, conduction bands, and color centers (Clark, 1999; Goetz, 1989). The electronic transitions require higher energy levels, and therefore occur at shorter wavelength regions compared to the vibrational processes (Goetz, 1989). Electronic transitions tend to dominate mineral spectra in the visible and NIR, but are also found across the SWIR region.

Vibrational processes cause spectral features from the SWIR to beyond the TIR (Hunt, 1980), and result from vibrations in the crystal lattice of minerals. Vibrational processes include fundamental, as well as overtone and combination vibrations. Absorption features associated with fundamental vibrational processes vary with differences in the anion composition, bond strength, and crystal structure of the minerals. Vibrational processes produce particularly diagnostic absorption features in the spectra of hydroxyl, iron, carbonate and water-bearing minerals (Hunt, 1980; Clark, 1999).

In the 8-12 μm TIR region, fundamental vibrational processes produce spectral features in silicate spectra, and this spectral region is therefore sometimes known as the "Si-O stretching region" (Hook *et al*., 1994). The wavelength of the major absorption feature tends to shift to shorter wavelengths with increasing bond strength (Vincent and Thomson, 1971; Hunt and Salisbury, 1974). Furthermore, for silicate minerals, the

wavelength of the Si-O absorption feature varies from 11 to 9 μm, corresponding to minerals with chain, sheet, and framework structures (Hunt, 1980).

The distinctive spectral features of silicates, as well as other important spectral features of most non-silicate minerals, including the carbonates, sulfates, phosphates, oxides, and hydroxide mineral groups, demonstrate the tremendous potential of the TIR region for geological mapping. Combining information from TIR spectral emissivity with measurement of spectral reflectance in the 0.4-2.5 μm region, which is particularly good for discriminating clays, iron oxides, and iron hydroxides (Clark, 1999), should provide a more comprehensive overview of rock compositional information than using data from only one of the two regions (Rowan, 1998).

Despite the promise of integrating VNIR/SWIR and TIR imagery (Hook *et al.*, 1999), most previous research has focused on using only either VNIR/SWIR hyperspectral data (Crósta *et al.,* 1998; Kruse, 1988; Kruse *et al.,* 1993b), or TIR multispectral data (Collins, 1991; Hook *et al*., 1994; Rowan and Mars, 2003; Sabine *et al*., 1994) on their own, or at most, a comparison of data sets of different wavelength (Abrams and Hook, 1991). Very little attention has been paid to image analysis approaches that draw on both VNIR/SWIR hyperspectral and TIR multispectral data simultaneously.

This study investigates the potential value of integration of VNIR/SWIR hyperspectral analysis with TIR multispectral analysis, with the anticipation that such an approach should provide improved discrimination of a wide range of rocks and minerals. The research has three main components.

The first part, comprising the stand-alone paper included here as Chapter 2, is an analysis of simulated hyperspectral VNIR/SWIR and multispectral TIR data. Simulated data are particularly useful because not only are the makeup and true proportions of the constituent minerals in the simulated spectra known, but also the amount and type of noise can be controlled. The simulated data were used to test the improvement in classification accuracy when the combination of VNIR/SWIR hyperspectral and TIR multispectral data is used, compared to an analysis that uses only the VNIR/SWIR data, or TIR data, on their own. In addition, the simulated data were used to evaluate the performance of automatic information extraction algorithms, including the statistical classification algorithms of minimum distance and maximum likelihood classification (Richards, 1993), as well as the hyperspectral analysis techniques of spectral angle mapper (SAM) (Kruse *et al*., 1993a), binary encoding (Goetz, *et al.,* 1985), and spectral feature fitting (SFF) (Crowley *et al.,* 1989; Clark *et al.,* 1990).

The second independent paper, Chapter 3, uses aircraft imagery to extend the results of the study of simulated data to real world data. The data used were hyperspectral VNIR/SWIR Airborne Visible/Infrared Imaging Spectrometer (AVIRIS) and multispectral TIR MASTER (MODIS/ASTER Airborne Simulator) data of Cuprite, Nevada. Cuprite is particularly suited for testing geological remote sensing methods because a wide range of rock and alteration types is well exposed in a sparsely vegetated environment. As with the simulated data discussed in Chapter 2, the AVIRIS and MASTER data were used to test if the combination of VNIR/SWIR hyperspectral data and TIR multispectral data improves the accuracy of lithological mapping. SAM, SFF, minimum distance, and maximum likelihood classification methods were applied to

AVIRIS, MASTER, and the combined data, respectively. Comparisons of the relative accuracy of each method and data set offers insight into how spectral characteristics of minerals and rocks influence the nature of the optimal data sets and methods for discrimination of those minerals.

The third and final independent paper, Chapter 4, draws on the results of the simulated and real data analyses to develop a rule based system for classifying minerals and rocks. The rule based system employs a set of rules to determine, for each pixel independently, the optimal data sets (VNIR/SWIR hyperspectral data, TIR multispectral data, or both) and classifications methods (SFF, or SAM), to discriminate the minerals and rocks of the area. Thus the final classified image is a composite of different approaches applied to different wavelength regions.

Chapter 5 is a general conclusion linking the three independent papers. The potential value of integration of VNIR/SWIR hyperspectral data and TIR multispectral data is evaluated by comparing the results of the simulated and real data analysis, and evaluating the benefits of the rule based system approach. In addition, the relative strengths of the maximum likelihood, minimum distance, SFF and SAM classification methods are compared.

References

Abrams, M. J., & Hook, S. J. (1991). Combined use of TIMS and AVIRIS for alteration mapping: In *Proceedings of the third Thermal Infrared Multispectral Scanner (TIMS) Workshop*, JPL Publication 91-29, 54-64.

Clark, R. N. (1999). Spectroscopy of rocks and minerals, and principles of spectroscopy. In A. N. Rencz (Ed.), *Remote Sensing for the Earth Sciences: Manual of Remote Sensing,* 3rd Ed., Vol. 3, Chapter 1 (pp. 3-58). New York: John Wiley and Sons.

Clark, R. N., Gallagher, A. J., & Swayze, G. A. (1990). Material absorption band depth mapping of imaging spectrometer data using the complete band shape least-squares algorithm simultaneously fit to multiple spectral features from multiple materials. *Proceedings of the Third Airborne Visible/Infrared Imaging Spectrometer (AVIRIS) Workshop*, JPL Publication 90-54, 176-186.

Clark, R. N., Swayze, G. A., Livo, K. E., Kokaly, R. F., Sutley, S. J., Dalton, J. B., McDougal, R. R., & Gent, C. A. (2003). Imaging Spectroscopy: earth and planetary remote sensing with the USGS Tetracorder and expert systems. *Journal of Geophysical research* 108 (E12), 5131, doi:10.1029/2002JE001847.

Collins, A.H.,1991. Thermal infrared spectra and images of altered volcanic rocks in the Virginia Range, Nevada. *International Journal of Remote Sensing* 12(7): 1559-1574.

Crósta, A. P., C. Sabine, and J. V. Taranik, 1998. Hydrothermal alteration mapping at Bodie, California, using AVIRIS hyperspectral data. *Remote Sensing of Environment* 65:309-319.

Crowley, J. K., Brickey, D. W., & Rowan, L. C. (1989). Airborne imaging spectrometer data of the Ruby Mountains, Montana: mineral discrimination using relative absorption band-depth images. *Remote Sensing of Environment*, 29, 121-134.

Goetz, A. F. H. (1989). Spectral remote sensing in geology. In: G. Asrar (ed.) *Theory and Applications of Optical Remote Sensing*, John Wiley & Sons, Inc., New York, Chapter 12. pp. 491-526.

Goetz, A. F. H., Vane, G. J., Solomon, E., & Rock, B. N. (1985). Imaging spectrometry for earth remote sensing. *Science*, 211, 1147-1153.

Hook, S. J., Abbott, E. Grove, A., C., Kahle, A. B., & Palluconi, F. (1999). Use of multispectral thermal infrared data in geological studies. In: A. N. Rencz (ed.), *Remote Sensing for the Earth Sciences*: *Manual of Remote Sensing*, 3 ed, Vol. 3, Chapter 2 (pp. 59-110), New York: John Wiley and Sons.

Hook, S. J., Gabell, A. R., Green, A. A., & Kealy, P. S. (1992). A comparison of techniques for extracting emissivity information from thermal infrared data for geologic studies. *Remote Sensing of Environment*, 42, 123-135.

Hook, S. J., Karlstrom, K. E., Miller, C. F., & McCaffrey, K. J. W. (1994). Mapping the Piute Mountains, California, with thermal infrared multispectral scanner (TIMS) images. *Journal of Geophysical Research*, 99, 15,605-15,622.

Hunt, G. R., & Salisbury, J. W. (1974). Mid-infrared spectral behavior of igneous rocks. *Technical Report AFRCL-TR-75-0356*, US Air Force Cambridge Research Laboratory, Cambridge, MA.

Kahle, A. B. (1987). Surface emittance, temperature, and thermal inertia derived from thermal infrared multispectral scanner (TIMS) data for Death Valley, California. *Geophysics* 52, 858-874.

Kruse, F. A., 1988. Use of Airborne Imaging Spectrometer data to map minerals associated with hydrothermally altered rocks in northern Grapevine Mountains, Nevada and California, *Remote Sensing of Environment* 24(1): 31-51.

Kruse, F. A., Lefkoff, A. B., Boardman, J. B., Heidebrecht, K. B., Shapiro, A. T., Barloon, P. J., & Goetz, A. F. H. (1993a). The spectral image processing system (SIPS) – Interactive visualization and analysis of imaging spectrometer data. *Remote Sensing of Environment*, 44, 145-163.

Kruse, F. A., Lefkoff, A. B., & Dietz, J. B. (1993b). Expert system-based mineral mapping in Northern Death Valley, California/Nevada, Using the Airborne Visible/Infrared Imaging Spectrometer (AVIRIS). *Remote Sensing of Environment*, 44, 309-336.

Lyon, R. J. P. (1972). Infrared spectral emittance in geologic mapping: Airborne spectrometer data from Pisgah Crater, CA. *Science*, 175, 983-985.

Mueller, Richter, A., R., Habermeyer, M., Mehl, H., Dech, S., Kaufmann, H., Segl, K., Haschberger, P., & Strobl, P. (2003). ARES: a new reflective/emissive imaging spectrometer for terrestrial application: In *Proceedings of thirteen Airborne Visible/Infrared Imaging Spectrometer (AVIRIS) and Hyperion Workshop*, Jet Propulsion Laboratory, Pasadena, California.

Price, J. C. (1979). Surface temperature variations as measured by the Heating Capacity mapping Mission. *Proceedings of the Thirteenth International Symposium on*

*Remote Sensing of the Environ*ment (pp. 765-770). Ann Arbor, MI: Environmental Research Inst. of Michigan.

Richards, J. A. (1993). *Remote Sensing Digital Image Analysis: An Introduction*. New York: Springer-Verlag, 340p.

Rowan, L. C. (1998). Analysis of simulated advanced spaceborne thermal emission and reflection (ASTER) radiometer data of the Iron Hill, Colorado, study area for mapping lithologies. *Journal of Geophysical Research D: Atmospheres*, 103, 32,291-32,306.

Rowan, L. C. and J. C. Mars, 2003. Lithologic mapping in the Mountain Pass, California area using Advanced Spaceborne Thermal Emission and Reflection Radiometer (ASTER) data. *Remote Sensing of Environment* 84: 350-366.

Sabine, C., V.J. Realmuto, and J.V. Taranik, 1994. Quantitative estimation of granitoid composition from thermal infrared multispectral scanner (TIMS) data, Desolation Wilderness, northern Sierra Nevada, California. *Journal of Geophysical Research* 99(B3): 4261-4271.

Vane, G., R. O. Green, T. G. Chrien, H. T. Enmark, E. G. Hansen, and W. M. Porter, 1993. Airborne Visible/Infrared Imaging Spectrometer (AVIRIS). *Remote Sensing of Environment* 44: 127-143.

Vincent, R.K., & Thomson, F. J. (1971). Discrimination of basic silicate rocks by recognition maps processed from aerial infrared data. *Proceedings of the Seventh*

International Symposium on Remote Sensing Environment(pp. 245-251). Ann Arbor, MI: University of Michigan.

Warner, T. A. & Chen, X. (2001). Normalization of Landsat thermal imagery for the effects of solar heating and topography. *International Journal of Remote Sensing*, 22, 773-788.

Chapter 2. Simulated Data Analysis

Abstract

This paper investigates the potential impact of combining visible, near infrared (VNIR), and shortwave infrared (SWIR) hyperspectral and thermal infrared (TIR) multispectral data on the comparative accuracy of different classification methods for surface bedrock geological mapping. A series of simulated data sets based on the characteristics of hyperspectral AVIRIS and multispectral TIR MASTER sensors was created from surface reflectance and emissivity library spectra of 16 common minerals and rocks occurring in Cuprite, Nevada. System noise, illumination effects, the presence of vegetation, and spectral mixing were added to create the simulated data. Five commonly used classification algorithms, minimum distance, maximum likelihood classification, binary encoding, spectral angle mapper (SAM), and spectral feature fitting (SFF), were applied to all data sets. All the classification methods, excluding binary encoding, achieved nominal to significant improvement in overall accuracy when applied to the combined data sets in comparison to using only the AVIRIS data set. Furthermore, certain classification methods of the combined data sets showed a marked increase in individual rock or mineral class accuracies. Limestone, silicified rock, and muscovite, for instance, showed an improvement of almost 30 percent or greater in either producer's or user's accuracy using the combined data sets with SAM. SFF provided a great improvement in accuracy for limestone, quartz, and muscovite. In terms of overall comparative accuracy for the individual and the combined data sets, maximum likelihood classification showed the best performance. For the simulated AVIRIS data, SFF was generally superior to SAM, although the accuracy of SAM applied to the combined data

sets was slightly better than that of SFF. SAM applied to the combined data sets increased classification accuracy for some minerals and rocks which do not exhibit distinct absorption features in thermal infrared region, while for SFF, only the accuracy of minerals and rocks with characteristic absorption features in the TIR was improved.

Key Words: hyperspectral; multispectral; visible; near infrared; short wave infrared; thermal; simulated imagery; classification methods.

1. Introduction

Recent developments in VNIR/SWIR[1] hyperspectral and TIR multispectral remote sensing have greatly increased the potential for accurate geological mapping. Hyperspectral instruments, often referred to as imaging spectrometers, acquire image data simultaneously in many narrow, contiguous channels (Goetz *et al*., 1985), generally spanning the reflected solar portion of the electromagnetic spectrum (0.4 - 2.5 μm) (Vane *et al*., 1993). The spectral bandwidths of hyperspectral image bands are generally less than 25 nm, in order to facilitate the identification of diagnostic absorption features of minerals (Clark, 1999). Hyperspectral data have a significant advantage over conventional multispectral data, such as Landsat Thematic Mapper imagery, in that with hyperspectral data, minerals can be identified by comparisons with generic library spectra (Clark *et al.*, 2003). With hyperspectral data, it is therefore theoretically possible to map

[1] An unfortunate inconsistency has developed in the terms used by the remote sensing community for regions of the electromagnetic spectrum (Clark, 1999). In this study, the wavelength regions are defined as follows: **visible**: 0.4 – 0.7 μm, **near-infrared (NIR)**: 0.7 – 1.1 μm, **visible and near-infrared (VNIR)**: 0.4 – 1.1 μm, **short-wavelength infrared (SWIR)**: 1.1 – 2.5 μm, **mid-infrared** (**MIR)**: 3 – 5 μm**,** and **thermal infrared (TIR)**: 8 – 14 μm (Goetz, 1989; Hook *et al*., 2001).

the surface mineralogy of an area without acquiring any ground data from the particular site.

In contrast to the many bands of hyperspectral instruments, TIR multispectral sensors measure surface radiance in a small number of broad bands. TIR imagery provides important information regarding temperature, thermal inertia, and emissivity of ground materials (Price, 1979; Kahle, 1987; Warner and Chen, 2001). Surface emissivity is potentially the most useful thermal property, because it is an inherent characteristic of an object, and is independent of illumination intensity and local temperature. Emissivity is defined as the ratio of the emitted radiation to that of a blackbody at the same temperature (Hook *et al*., 1992). Emissivity can be used to identify individual minerals, and has been related to silica content of rocks (Lyon, 1972), thus offering the possibility of discriminating the silicate materials that make up much of the land surface.

Minerals tend to have characteristic spectral reflectance and associated emissivity features, which may potentially be used for remote identification (Clark, 1999; Hook *et al*., 1994). The characteristic spectral features are produced by the interaction of electromagnetic energy with the atoms and molecules of the minerals, which cause electronic transitions and vibrational processes. Electronic transitions tend to dominate mineral spectra in the visible and NIR, but are also found across the SWIR region (Clark, 1999; Goetz, 1989). Vibrational processes, dominating in SWIR and TIR region, produce particularly diagnostic absorption features in the spectra of silicate, hydroxyl, oxide, carbonate and water-bearing minerals (Vincent and Thomson, 1971; Hunt and Salisbury, 1974; Hunt, 1980; Hook *et al*., 1994; Clark, 1999).

The distinctive spectral features of silicates, as well as other important spectral features of most non-silicate minerals, including the carbonates, sulfates, phosphates, oxides, and hydroxide mineral groups, demonstrate the tremendous potential of the TIR region for geological mapping. Combining information from TIR spectral emissivity with measurement of spectral reflectance in the 0.4-2.5 μm region, which is particularly good for discriminating clays, iron oxides, and iron hydroxides (Clark, 1999), should provide a more comprehensive overview of rock compositional information than using data from only one of the two regions (Rowan, 1998).

In summary, the combination of VNIR/SWIR hyperspectral data and TIR multispectral data appears to have great promise for geological studies because of the complementary nature of information from the thermal and shorter wavelengths (Hook *et al.*, 1999). Typically, iron oxide, hydroxyl, and carbonate minerals have absorption features in the visible or SWIR region, while the Si-O bonding of silicate minerals exhibit absorption features in TIR region. Nevertheless, combining VNIR/SWIR and TIR data has received very little prior attention, with the exception of Abrams and Hook (1991), who separately analyzed VNIR/SWIR hyperspectral and TIR multispectral data for lithological analysis at Cuprite, Nevada.

That no previous research has simultaneously analyzed VNIR/SWIR hyperspectral and TIR multispectral data is probably due to the fact that data from these spectral regions are rarely acquired simultaneously, and that coregistration of aerial imagery from different sources can be very challenging. However, modern aircraft-acquired data often include navigation information that can be used to remove non-systematic spatial distortions. Furthermore, in the future, with the increased availability

of satellite data, which tends to have simpler geometry than aerial imagery, coregistration of different image products may become more routine. In fact, space-borne hyperspectral data is already being collected by the Hyperion instrument, and space-borne multispectral TIR data by the Advanced Spaceborne Thermal Emission and Reflection Radiometer (ASTER). Integrating imagery from different sensors may not even be necessary in the future; for example there are plans to fly an airborne hyperspectral sensor in 2005, Airborne Reflective Emissive Spectrometer (ARES), which has 160 image bands in the visible, NIR, SWIR, and TIR wavelength regions (Mueller *et al*., 2003).

This study investigated the potential value of integration of VNIR/SWIR hyperspectral analysis with TIR multispectral analysis, with the anticipation that such an approach should provide improved geological mapping. To test this hypothesis, simulated data were used to test the improvement in classification accuracy when the combination of VNIR/SWIR hyperspectral and TIR multispectral data is used, compared to an analysis that uses only the VNIR/SWIR or TIR regions on their own. In addition, the simulated data were used to evaluate the performance of automatic information extraction algorithms, including the conventional classification algorithms of minimum distance and maximum likelihood classification (Richards, 1993), as well as the hyperspectral analysis techniques of spectral angle mapper (Kruse *et al*., 1993a), binary encoding (Goetz, *et al.,* 1985), and spectral feature fitting (Crowley *et al.,* 1989; Clark *et al.,* 1990).

Simulated data have been demonstrated to be useful in developing general theories about how information is represented in images and spectra (Strahler *et al.*, 1986). For example, simulated data have been used in many studies of image spatial

properties (e.g. Woodcock *et al.*, 1988, Jupp *et al.*, 1989, Collins and Woodcock, 1999, Warner, 1999, Ferro and Warner, 2002), and spectral properties (e.g. Verhoef, 1984, Li *et al*., 1999, Pandya *et al*., 2000).

Simulated data were chosen for this study because with simulated data it is possible to evaluate accuracy with complete confidence in the reference data set. A geological map is always complex and heterogeneous. Ground checking of minerals for real hyperspectral analyses is challenging, especially when the minerals are fine grained. Although minerals can be identified through laboratory techniques, it is hard to generalize from small laboratory samples to 20 meter pixels, and especially difficult to estimate the proportions of minerals present in fine mixtures. Additional uncertainty is added by varying desert varnish, vegetation, weathering, and deposition of transported material in each pixel. Thus, in summary, it is close to impossible to produce a "truth map" for geological hyperspectral remote sensing. Perhaps most telling is that we know of no previous quantitative assessment of accuracy of geological hyperspectral remote sensing classification.

A second reason for using simulated data is that this approach allows us to vary image properties in a controlled fashion, and thus potentially develop an understanding of the reasons behind the results we observe. We are also able to study what aspects of the scene model most affect the different methods, a key to developing improvements to the different methods. For example, if illumination variation were found to be a major source of error, then we would infer that illumination normalization methods should be researched further.

The third reason for using simulated data is that simulation provides a simplified, but reasonable, representation of real data as long as the major processes that result in a real image are included in the analysis. Simulated data are typically much simpler than reality. This does not necessarily negate the value of simulated data; indeed, the simplification can be an advantage, as discussed above.

In Chapter 3, the classification methods tested in this paper will be applied to real data, comprising AVIRIS (Airborne Visible/Infrared Imaging Spectrometer) and MASTER (MODIS/ASTER Airborne Simulator) imagery of Cuprite, Nevada.

2. Methods

2.1 Classification algorithms

Image classification methods can be divided into two groups: **empirical classification algorithms** that use summary class statistics based on groups of image pixels, and **spectral analysis techniques** that match image spectra to previously acquired field or laboratory spectra, known as spectral libraries. With hyperspectral data, empirical classification approaches that rely on second order statistical measures tend to require excessive numbers of training samples for training the classifier (Landgrebe, 2000). The spectral library approach is attractive for hyperspectral image analysis because rocks and minerals tend to have distinctive and consistent spectral absorption features, as discussed above. Furthermore, the potential to identify surface materials without any local field data is clearly very attractive.

The two most common empirical classification methods used for geological mapping are minimum distance and maximum likelihood classification. Numerous

additional spectral analysis methods have been developed for geological mapping (Mustard and Sunshine, 1999), including binary encoding, spectral feature fitting, and the spectral angle mapper. These three spectral analysis methods will be described briefly below.

Binary encoding (Goetz, *et al.,* 1985) is a fast spectral matching algorithm that compares summary measures of the spectral shapes of an unknown pixel and the reference spectra. The unknown pixel spectrum of *n* bands is represented by an *n* bit vector, with each bit set to 1 or 0 respectively, depending on whether the value of the spectrum for that band is above or equal to, or below the pixel mean. Because of its simplicity, binary encoding is often used as a provisional, or exploratory, classification approach. Nevertheless, binary encoding is included in this study to give a wider representation of hyperspectral analysis methods.

Spectral feature fitting (SFF) (Crowley *et al.,* 1989; Clark *et al.,* 1990) is based on a comparison of the absorption features in the image and reference spectra. The continuum, defined as a convex hull fit over the top of each spectrum utilizing straight line-segments to connect local spectrum maxima (Clark *et al*., 2003, Kruse *et al.,* 1993b), is removed by dividing the convex hull into the original spectrum. The continuum-removed pixel spectrum and reference spectra are compared at each absorption band using a least-square fit. The root mean square error indicates the relative goodness-of-fit of the two spectra.

Spectral angle mapper (SAM) (Kruse *et al*., 1993a) builds on the hyperspherical direction cosine method (Pouch and Campagna, 1990) by calculating the similarity

between pixel spectra and reference spectra in terms of the angle between two *n*-dimensional vectors, where *n* is the number of bands of hyperspectral data.

2.2 Simulated data

The creation of the simulated data was carried out using the Interactive Data Language (IDL) (Research Systems, 2004a). The spectra of 16 common minerals, rock types, and alteration types (Table 2.1) were chosen for this study because they represent the dominant lithological units and alteration types typical of hydrothermal alteration areas such as Cuprite, Nevada (Abrams and Ashley, 1980). The mineral spectra selected were those with the finest grain size; for rocks and the three alteration types, a solid surface was measured. All fine grained mineral spectra used have a relative low contrast, and they are the most representative of the ground surface in reality. The spectra were resampled to match the approximate spectral bandwidth and signal-to-noise of the AVIRIS and MASTER instruments. A brief introduction to the AVIRIS and MASTER instruments is given below (see also Table 2.2), followed by a more detailed discussion of the simulated data characteristics.

The MASTER sensor was developed to support research prior to the launch of the Advanced Spaceborne Thermal Emission and Reflection Radiometer (ASTER) and the Moderate Resolution Imaging Spectroradiometer (MODIS) (Hook *et al*., 2001). MASTER has a total of 50 bands from 0.4-13 μm, including 10 TIR bands. In this study, simulated multispectral thermal data are based only on the 10 MASTER TIR bands (7.6-13 μm). AVIRIS, flown by NASA since 1987 (Green *et al*., 1998), acquires data in 224 narrow, contiguous spectral bands across the reflected solar energy region (0.4-2.5 μm), each band approximately 10 nm at full width, half maximum (FWHM).

The simulated data for the nine minerals and the four unaltered rocks (Table 2.1) were derived from the public domain spectral library included with ENVI (Research Systems, 2004b): the Johns Hopkins University library of spectra of materials from 0.4 to 14 μm (Salisbury *et al*., 1991; Research Systems, 2004b). The simulated data for the three hydrothermally altered rocks were derived from spectral measurements of samples collected at Cuprite. The original rocks of hydrothermal alteration ranged from intrusive rock to volcanic tuffs. Silicified rock, the most intensive alteration, contain abundant quartz and some other minerals such as calcite, alunite, and kaolinite; opalized rock is the moderate altered type, presenting opal and variable amounts of alunite and kaolinite; argillized rock is the least altered type consisting of primary quartz, altered montmorillonite and kaolinite (Abrams and Ashley, 1980). For the altered rocks, the spectra from 0.4 to 2.5 μm were measured by the author with an Analytical Spectral Devices (Boulder, Colorado) field portable spectrometer, FieldSpec Pro Full Range, and the spectra from 2 to 14 μm were measured with a Fourier Transform Infrared Spectrometer (FTIR) at NASA's Jet Propulsion Laboratory (JPL). The Emissivities of minerals or rocks are calculated from Kirchoff's law, which states that spectral emissivity equals 1 minus the spectral reflectance.

To simplify the simulated data construction, the contribution of the atmosphere was not modeled directly. Nevertheless, the effects of the atmosphere were included indirectly, because noise equivalent to that found in typical AVIRIS and MASTER scenes that include atmospheric effects, was added on a band-by-band basis. In addition, the simulated AVIRIS bands in the atmospheric water absorption regions near 1.4, 1.9, and 2.5 μm were deleted, leaving a total of 188 out of the 224 bands for the analysis.

Multiplying the spectral radiances with the inverse of the spectral signal-to-noise ratios for AVIRIS and MASTER simulated the noise of the sensor system. The signal-to-noise ratio of AVIRIS was estimated using the ratio of the mean and standard deviation of a 3 by 3 window of pixels from an AVIRIS image of a playa in Luna Lake, Nevada acquired on Jun. 23, 1997. The signal-to-noise ratio of MASTER was calculated in the same way using a MASTER image of Lake Mead, Nevada acquired on Sep. 20, 1999. An additional 0.015 variation in emissivity (Gillespie *et al.,* 1998) was added to simulate the uncertainty due to the indeterminacy of the emissivity calculation from radiance data.

The library spectra were also combined in various proportions to simulate real pixels, which generally comprise mixed proportions of different surface materials:

$$L_\lambda = \sum_{i=1}^{n} (a_i R_{\lambda i}) + \varepsilon_\lambda \qquad (1)$$

Where

L_λ = reflectance or emissivity at wavelength λ corresponding to a specific AVIRIS or MASTER band;

a_i = the proportion of the endmember i in the pixel;

$R_{\lambda i}$ = the reflectance or emissivity of endmember i at wavelength λ;

ε_λ = the error term resulting from all sources of noise at wavelength λ.

Seven groups of simulated data with different levels of uncertainties were derived using equation 1 (Table 2.3). Each group includes three data sets designed to simulate AVIRIS data (188 bands between 0.4 -2.5 μm, after the exclusion of the water absorption bands), MASTER thermal data (10 bands between 7.6 -13 μm), and the combination of AVIRIS and MASTER multispectral thermal infrared data (a total of 198 bands between

0.4 -2.5 μm and 7.6 -13 μm). The simulated uncertainties include sensor system noise, mixing of vegetation and the other endmembers, and variation in solar illumination. Solar illumination effects were simulated by varying the total radiance by 0 to 20 percent. The first group of data is a theoretical near-perfect data set, containing only reflectance or emissivity information and system noise of sensor instruments. The uncertainties of the second group include the system noise and solar illumination effects; in the third group, solar illumination effects and a random percentage of vegetation, up to 5 percent, is added; the fourth group has solar illumination effects, a random proportion, up to 5 percent, vegetation, and up to10 percent of another mineral or rock endmember, randomly selected from the 16 library spectra; the fifth group is similar to the fourth except up to 10 percent of vegetation; the sixth group has up to 10 percent vegetation and up to 20 percent of another mineral or rock endmember, and the illumination effects; the seventh group has up to 10 percent vegetation, up to 30 percent another endmember, and illumination effects.

2.3 Analysis

All classification and spectral analysis methods were carried out with ENVI image analysis software (Research System, 2004b). Binary encoding, SAM, and SFF were applied using endmember spectra derived from training data. SFF is normally used with data of more limited spectral regions, and therefore SFF was also tested using the simulated AVIRIS bands from just the SWIR region (1.96 – 2.44 μm). Considering that SFF's focus on spectral absorption features makes the method inappropriate for use with minerals and rocks with spectrally flat curves, additional comparisons were made using only the nine minerals which exhibit absorption features in VNIR, SWIR: alunite,

argillized rock, calcite, goethite, hematite, kaolinite, montmorillonite, opalized rock, and gypsum.

Data sets 5, 6 and 7 have comparatively high levels of uncertainty, and were found to produce notably low accuracies, especially for minimum distance and binary encoding classification. Therefore, additional preprocessing was carried out to evaluate whether the effect of the uncertainty could be reduced for these methods using the minimum noise fraction (MNF) transformation **(**Green *et al*., 1988). MNF was used to generate 15 MNF bands for each data set. MNF consists of two cascaded principal component transformations, and is usually used to suppress noise and reduce the number of bands prior to classification. The first transformation decorrelates and rescales the noise in the data, assuming the noise has unit variance and no band-to-band correlation. The second step is a standard principal component transformation applied on the noise-free data. The final transformed data includes two parts: one part associated with large eigenvalues representing most of the variance, and a second part with near-unity eigenvalues representing the noise-dominated data **(**Green *et al*., 1988).

Overall accuracies were calculated, and used to evaluate the degree to which the combined data aids discrimination by contributing to increased separability of the entire group of spectral classes. ENVI's confusion matrix procedure (Research Systems, 2004b) was applied to all classified images to evaluate the performance of the classifications. The same approximately 10,000 pixels used for training the classifiers were used for classification assessment. In conventional accuracy assessment, different training and testing pixels are normally used. However, in this case, with a large random sample, there would be little difference in the results if a new data set was used for

testing. In confusion matrix, two parameters, producer's accuracy and user's accuracy were used to indicate the classification accuracy of each mineral or rock. Producer's accuracy is defined as the probability that a pixel is classified as class A given that ground truth is class A. User's accuracy indicates the percentage of the number of correctly classified pixel of certain class among the total number of pixel classified as that class (Research Systems, 2004b).

3. Results

3.1. Evaluation of combining VNIR, SWIR, and TIR spectral regions

The overall accuracies of classification (Figure 2.1) were found to vary with the mapping methods and the data sets. Figure 2.1 provides evidence to support the hypothesis that the combination of AVIRIS and MASTER aids discrimination of minerals and rocks. First, for all classification methods except binary encoding, the combined data set always has the highest overall accuracy of the three data sets. The combined data set also produced the highest accuracy for minimum distance classification and binary encoding applied to MNF transformed data (Figure 2.2).

When the classifications are examined in more detail, some of the individual minerals and rocks can be seen to show large improvement in classification accuracy when the AVIRIS data set was combined with the MASTER data set (Table 2.4). For instance, limestone, muscovite, and silicified rock showed an improvement of almost 30 percent in either the producer's accuracy or the user's accuracy when SAM was applied to the combined data set. However, some minerals and rocks, such as alunite, basalt, and kaolinite, showed little improvement, or even a decrease in accuracy. Most of the

minerals that showed an improvement in classification accuracy with the combined data sets analyzed using SFF classification exhibit characteristic absorption features in the thermal infrared wavelength region (Figure 2.3 right). For example, quartz and muscovite, which have deep Si-O features around 9 μm (Figure 2.3 right), generally showed a marked improvement in classification accuracy using the combined data set (Table 2.4). Likewise, silicified alteration showed a higher classification accuracy with the combined data set because it has relative strong features at 9 μm (Figure 2.4 right). In the VNIR and SWIR regions, basalt and limestone have similar very flat spectra (Figure 2.4 left). These two classes were poorly differentiated and both showed high omission and commission error. However, limestone has a weak feature around 11 μm which improved discrimination once MASTER TIR data was combined with the AVIRIS data. On the other hand, basalt and sandstone have relatively flat TIR spectra (Figure 2.4 right), so combining AVIRIS and MASTER wavelength reduced their classification accuracies. Calcite has only two relative weak features in the 9 and 11 μm wavelength regions (Figure 2.3), which are diluted by mixing with other minerals or rocks. Therefore, calcite did not show much improvement in classification accuracy with the combined data set. Although alunite and gypsum are characterized by strong features in the TIR, they are too similar to be separated in the MASTER data, and therefore the combined data set did not enhance discrimination.

When SFF was applied to the AVIRIS SWIR bands alone (1.96 – 2.44 μm), the overall accuracy decreased, although some minerals with distinctive absorption features in the SWIR region, such as alunite and calcite (Figure 2.3 left), showed slight improvement in user's accuracy (Table 2.5). However, some minerals with characteristic

absorption features in the VNIR region, for instance, hematite and goethite (Figure 2.3 left), showed a large decrease in accuracy. Thus, as might be expected, SFF applied to a relatively narrow wavelength region only enhances identification of the specific minerals or rocks which exhibit distinctive absorption features in that wavelength region.

3.2. Evaluation of classification algorithms

The major uncertainties added to the data sets include variable vegetation coverage, solar illumination effects, and mixing of the other minerals (Table 2.3). All the classification methods, with the exception of maximum likelihood classification applied to the simulated AVIRIS data sets, are generally sensitive to the type and degree of uncertainty. For the near-perfect data set of the simulated AVIRIS with only instrumental system noise, all methods achieved almost 100 percent classification accuracies (Figure 2.1). When up to 5 percent mixing of vegetation and solar illumination effects were added to the data (Uncertainty Level 3), maximum likelihood classification, SAM, and binary encoding still resulted in 100 percent accuracy; the accuracy of SFF decreased slightly, and the accuracies using the minimum distance classification dropped notably. This suggests that minimum distance classification is very sensitive to illumination variation, as might be expected. With the increase of mixing uncertainty, maximum likelihood classification still showed almost 100 percent accuracy, whereas SAM and SFF decreased slowly and binary encoding and minimum distance classification decreased relatively rapidly. Although the overall accuracy of SAM dropped by 20 percent for uncertainty class 7, it nevertheless obtained the second highest accuracy. In terms of overall accuracy of the different methods, maximum likelihood classification is the best method for minerals and rocks classification using the

simulated AVIRIS data (Figure 2.1, top left), followed by SAM, then SFF; binary encoding and minimum distance classification have relative poor performance.

The results of the combined simulated data sets differ slightly from those of the simulated AVIRIS data (Figure 2.1, top right). In terms of overall accuracy, maximum likelihood classification almost achieved 100 percent accuracy for all uncertainty level data sets, and SFF resulted in the second highest accuracy for data sets 3 and 4. For data sets 5, 6, 7, the accuracy of the SFF method dropped to the third position. Minimum distance classification and binary encoding resulted in the lowest accuracies. Curves of minimum distance and maximum likelihood classification accuracy versus uncertainty follow the same trend as those of the AVIRIS data set, but the relative accuracies of the other methods differ greatly. Binary encoding applied to data sets 2, 3, and 4, for the combination of simulated AVIRIS and MASTER TIR data generally showed a reduction in accuracy. The performances of SAM and SFF are very close for the combined data sets. It appears that for the combined data these two methods are not sensitive to moderate mixing uncertainty.

SFF resulted in the third lowest accuracy, less then 50 percent, for the simulated MASTER data (Figure 2.1, bottom). This poor result suggests that, as might be expected, SFF is not good for classifying multispectral data with relative broad bandwidths, like MASTER data.

It is notable that maximum likelihood classification achieved the best performance on all data sets. Factors in the simulated data analysis that favor the maximum likelihood classification is the large and representative training sample of approximately 10,000 pixels, and that uncertainty in the data sets were modeled with

normal distributions. In real applications, it can be difficult to select sufficiently large samples of training data that completely characterize the classes of interest, and variability does not necessarily follow a normal distribution.

When the minerals and rocks with no distinct absorption features in the VNIR and SWIR regions are excluded from the analysis, leaving just 9 minerals, the average results of SAM, SFF, and binary encoding (Figure 2.5) are similar in trend to the average results found with all 16 minerals and rocks (Figure 2.1), although in detail there are some important differences. Excluding the classes with relatively flat spectral curves, including basalt, quartz, limestone, muscovite, sandstone, siltstone, and silicified alteration, raised the accuracy of most methods, especially SFF. In fact, SFF achieved the highest position in relative overall accuracy applied to the simulated AVIRIS data for the 9 minerals for all uncertainty classes (Figure 2.5, left). Applied to the combined data sets, SAM resulted in the best classification accuracy. Thus, as has been commented on before, SFF is not suitable for discriminating minerals with limited or no absorption features in the TIR wavelength region, such as kaolinite and montmorillonite.

4. Summary and conclusions

A series of simulated data sets based on the characteristics of AVIRIS and MASTER sensors was created. The simulated data sets include surface reflectance and emissivity derived from library spectra of 16 common minerals and rocks occurring in Cuprite, Nevada. Five automatic classification algorithms, minimum distance, maximum likelihood classification, binary encoding, SAM, and SFF, were applied to all data sets.

The classification results showed that combining AVIRIS with MASTER data sets can be useful for improving the accuracy of identifying the 16 selected minerals and

rocks in some circumstances. First, most methods applied to the combined data sets, except binary encoding, achieved varying improvement in overall accuracy in comparison to these methods used with the AVIRIS data set alone. Second, some minerals and rocks showed a great improvement in their individual classification accuracies. For instance, quartz, silicified alteration, limestone, and muscovite showed an improvement of at least 30 percent or greater in either the producer's or the user's accuracy using the combined data sets with SAM and with SFF. Because SFF is an absorption feature based method, the combination of AVIRIS with MASTER with SFF only enhances discrimination of minerals and rocks exhibiting distinctive features in the TIR region. Within the 16 minerals and rocks, only gypsum, alunite, quartz, muscovite, silicified alteration, and opalized alteration, have distinctive features in the TIR region. Adding uncertainty to MASTER tends to dilute absorption features. Therefore, for some minerals and rocks, combining MASTER TIR with AVIRIS bands degrades the performance of SFF.

Almost all methods used in this study are sensitive to mixing uncertainty. The only exception is maximum likelihood classification, at least within the constraints of this study. SAM and SFF applied to the data set consisting of minerals exhibiting distinctive absorption features was found to be relative tolerant to mixing uncertainty. SAM, binary encoding, and SFF are less sensitive to illumination effects when they are applied to the simulated AVIRIS data sets. Maximum likelihood classification is relatively robust in the presence of uncertainties, at least if sufficient training samples can be identified to estimate the probability distribution accurately. Generally however, it may not be possible to find a sufficient number of training pixels for the high dimensionality of

AVIRIS data. Therefore, it may be necessary to perform feature extraction, for example the MNF transformation, on the simulated AVIRIS and combined data sets before maximum likelihood classification is applied. The accuracy of minimum distance classification and binary encoding on MNF transformed data sets was almost 100 percent, indicating that the performance of MNF is very successful in suppressing the noise, and reducing the number of bands, at least for these simulated data.

In terms of overall accuracy of classification, maximum likelihood classification showed the best performance. However, prior knowledge about the study area is required in order to select training samples. Hyperspectral analysis methods like SFF have an advantage over maximum likelihood classification in that, at least potentially, external library spectra can replace in-scene training data. The simulated AVIRIS data showed that SFF is generally superior to SAM, although the accuracy of SAM applied to combined data sets is slightly better than that of SFF. SAM applied to the combined data sets increased classification accuracy for some minerals and rocks which do not exhibit distinct absorption feature in thermal infrared region, while for SFF, only the accuracy of minerals and rocks with characteristic absorption features in thermal infrared region was improved. Although binary encoding and minimum distance classification showed a relative poor performance on the simulated AVIRIS and combined data sets, binary encoding has some advantages, including a relatively simple algorithm, it is very fast, and is insensitive to illumination variation. Minimum distance classification is also relatively fast, only needs a small number of training samples, and achieves very high accuracy when it is applied to multispectral data sets. SFF is not good for multispectral data,

whereas SAM can achieve relatively good performance with either hyperspectral or multispectral data.

Acknowledgments

The authors would like to thank Dr. S. J. Hook and Dr. R. O. Green for advice on calculation of the signal-to-noise ratio of MASTER TIR and AVIRIS data respectively, and Cindy Grove of the Jet Propulsion Laboratory for measuring the spectra of field collected samples. Support for this research was provided by West Virginia View.

References

Abrams, M. J., & Ashley, R. P. (1980). Alteration mapping using multispectral images – Cuprite Mining District, Esmeralda County, Nevada. *U. S. Geological Survey Open File Report,* 80-367.

Abrams, M. J., & Hook, S. J. (1991). Combined use of TIMS and AVIRIS for alteration mapping: In *Proceedings of the third Thermal Infrared Multispectral Scanner (TIMS) Workshop*, JPL Publication 91-29, 54-64.

Clark, R. N. (1999). Spectroscopy of rocks and minerals, and principles of spectroscopy. In A. N. Rencz (Ed.), *Remote Sensing for the Earth Sciences: Manual of Remote Sensing,* 3 ed, Vol. 3, Chapter 1 (pp. 3-58). New York: John Wiley and Sons.

Clark, R. N., Gallagher, A. J., & Swayze, G. A. (1990). Material absorption band depth mapping of imaging spectrometer data using the complete band shape least-squares algorithm simultaneously fit to multiple spectral features from multiple materials.

Proceedings of the Third Airborne Visible/Infrared Imaging Spectrometer (AVIRIS) Workshop, JPL Publication 90-54, 176-186.

Clark, R. N., Swayze, G. A., Livo, K. E., Kokaly, R. F., Sutley, S. J., Dalton, J. B., McDougal, R. R., & Gent, C. A. (2003). Imaging Spectroscopy: earth and planetary remote sensing with the USGS Tetracorder and expert systems. *Journal of Geophysical research* 108 (E12), 5131, doi:10.1029/2002JE001847.

Collins, J. B., & Woodcock, C. E. (1999). Geostatistical estimation of resolution dependent variance in remotely sensed images. *Photogrammetric Engineering and Remote Sensing*, 65, 41-50.

Crowley, J. K., Brickey, D. W., & Rowan, L. C. (1989). Airborne imaging spectrometer data of the Ruby Mountains, Montana: mineral discrimination using relative absorption band-depth images. *Remote Sensing of Environment*, 29, 121-134.

Ferro, C. J. & Warner, T. A. (2002). Scale and texture in digital image classification. *Photogrammetric Engineering and Remote Sensing,* 68, 51-63.

Gillespie, A.R., Rokugawa, S., Matsunaga, T., Cothern, J. S., Hook, S., & Kahle, A. B. (1998). A temperature and emissivity separation algorithm for advanced spaceborne thermal emission and reflection radiometer (ASTER) images. *IEEE Transactions on Geoscience and Remote Sensing*, 36, 1113-1126.

Goetz, A. F. H. (1989). Spectral remote sensing in geology. In: G. Asrar (ed.) *Theory and Applications of Optical Remote Sensing*, John Wiley & Sons, Inc., New York, Chapter 12. pp. 491-526.

Goetz, A. F. H., Vane, G. J., Solomon, E., & Rock, B. N. (1985). Imaging spectrometry for earth remote sensing. *Science*, 211, 1147-1153.

Green, A. A., Berman, M., Switzer, P., & Craig, M. D. (1988). A transformation for ordering multispectral data in terms of image quality with implications for noise removal. *IEEE Transactions on Geoscience and Remote Sensing*, 26, 65-74.

Green, R. O., Eastwood, M. L., Sarture, C. M., Chrien, T., Aronsson, G. M., Chippedale, B. J., Faust, J. A., Pavri, B. E., Chovit, C. J., Solis, M., Olah, M. R., & Williams, O. (1998). Imaging Spectroscopy and the Airborne Visible/Infrared Imaging Spectrometer (AVIRIS). *Remote Sensing of Environment*, 65, 227-248.

Hook, S. J., Abbott, E. Grove, A., C., Kahle, A. B., & Palluconi, F. (1999). Use of multispectral thermal infrared data in geological studies. In: A. N. Rencz (ed.), *Remote Sensing for the Earth Sciences*: *Manual of Remote Sensing*, 3 ed, Vol. 3, Chapter 2 (pp. 59-110), New York: John Wiley and Sons.

Hook, S. J., Gabell, A. R., Green, A. A., & Kealy, P. S. (1992). A comparison of techniques for extracting emissivity information from thermal infrared data for geologic studies. *Remote Sensing of Environment*, 42, 123-135.

Hook, S. J., Karlstrom, K. E., Miller, C. F., & McCaffrey, K. J. W. (1994). Mapping the Piute Mountains, California, with thermal infrared multispectral scanner (TIMS) images. *Journal of Geophysical Research*, 99, 15,605-15,622.

Hook, S. J., Myers, J. J., Thome, K. J., Fitzgerald, M., & Kahle, A. B. (2001). The MODIS/ASTER Airborne Simulator (MASTER) – a new instrument for earth science studies. *Remote Sensing of Environment*, 76, 93-102.

Hunt, G. R. (1980). Electromagnetic radiation: the communication link in remote sensing. In B.S. Siegal and A.R. Gillespie (eds.), *Remote Sensing in Geology* (pp. 5-45). New York: Wiley.

Hunt, G. R., & Salisbury, J. W. (1974). Mid-infrared spectral behavior of igneous rocks. *Technical Report AFRCL-TR-75-0356*, US Air Force Cambridge Research Laboratory, Cambridge, MA.

Jupp, D. L., Strahler, A. H. & Woodcock, C. E. (1989). Autocorrelation and regularization in digital images. II. Simple image models. *IEEE Transactions on Geoscience and Remote Sensing*, 27, 247-258.

Kahle, A. B. (1987). Surface emittance, temperature, and thermal inertia derived from thermal infrared multispectral scanner (TIMS) data for Death Valley, California. *Geophysics* 52, 858-874.

Kruse, F. A., Lefkoff, A. B., Boardman, J. B., Heidebrecht, K. B., Shapiro, A. T., Barloon, P. J., & Goetz, A. F. H. (1993a). The spectral image processing system (SIPS) – Interactive visualization and analysis of imaging spectrometer data. *Remote Sensing of Environment*, 44, 145-163.

Kruse, F. A., Lefkoff, A. B., & Dietz, J. B. (1993b). Expert system-based mineral mapping in Northern Death Valley, California/Nevada, Using the Airborne

Visible/Infrared Imaging Spectrometer (AVIRIS). *Remote Sensing of Environment*, 44, 309-336.

Landgrebe, D. (2000). Information extraction principles and methods for multispectral and hyperspectral image data. In C. H. Chen (ed.), *Information Processing for Remote Sensing,* Chapter 1, NJ.: World Scientific Publishing Co., Inc., River Edge.

Li, Z., Becker, F., Stoll, M. P., & Wan, Z. (1999). Evaluation of six methods for extracting relative emissivity spectra from thermal infrared images. *Remote Sensing of Environment*, 69, 197-214.

Lyon, R. J. P. (1972). Infrared spectral emittance in geologic mapping: Airborne spectrometer data from Pisgah Crater, CA. *Science*, 175, 983-985.

Mueller, Richter, A., R., Habermeyer, M., Mehl, H., Dech, S., Kaufmann, H., Segl, K., Haschberger, P., & Strobl, P. (2003). ARES: a new reflective/emissive imaging spectrometer for terrestrial application: In *Proceedings of thirteen Airborne Visible/Infrared Imaging Spectrometer (AVIRIS) and Hyperion Workshop*, Jet Propulsion Laboratory, Pasadena, California.

Mustard, J. F. & Sunshine, J. M. (1999). Spectral analysis for earth science: Investigations using remote sensing data. In A. N. Rencz (Ed.), *Remote Sensing for the Earth Sciences*: Manual of Remote Sensing, 3 ed, Vol. 3, Chapter 5 (pp. 251-306), New York: John Wiley and Sons.

Pandya, M. R., Dadhwal, V. K., & Navalgund, R. R. (2000). Effects of WiFS viewing geometry on crop reflectance: A simulation study using SAIL model. International Journal *of Remote Sensing*, 21, 1931-1938.

Pouch, G. W. & Campagna, D. J. (1990). Hyperspherical direction cosine transformation for separation of spectral and illumination information in digital scanner data. Photogrammetric *Engineering and Remote Sensing*, 56, 475-479.

Price, J. C. (1979). Surface temperature variations as measured by the Heating Capacity mapping Mission. *Proceedings of the Thirteenth International Symposium on Remote Sensing of the Environ*ment (pp. 765-770). Ann Arbor, MI: Environmental Research Inst. of Michigan.

Richards, J. A. (1993). *Remote Sensing Digital Image Analysis: An Introduction*. New York: Springer-Verlag, 340p.

Research Systems (2004a). *Using IDL, IDL Version 6.1*. Research Systems, Boulder CO, 736p.

Research Systems (2004b). *ENVI User's Guide, ENVI 4.1*. Research Systems, Boulder CO, 1050p.

Rowan, L. C. (1998). Analysis of simulated advanced spaceborne thermal emission and reflection (ASTER) radiometer data of the Iron Hill, Colorado, study area for mapping lithologies. *Journal of Geophysical Research D: Atmospheres*, 103, 32,291-32,306.

Salisbury, J. W., Walter, L. S., Vergo, N., & D`Aria, D. M. (1991). *Infrared (2.1-25 micrometers) Spectra of Minerals*. Johns Hopkins University Press, 294p.

Strahler, A. H., Woodcock, C. & Smith, J. A. (1986). On the nature of models in remote sensing. *Remote Sensing of Environment* 20, 121-139.

Vane, G., Green, R. O., Chrien, T. G., Enmark, H. T., Hansen, E. G., & Porter, W. M. (1993). Airborne Visible/Infrared Imaging Spectrometer (AVIRIS). *Remote Sensing of Environment*, 44, 127-143.

Verhoef, W. (1984). Light scattering by leaf layers with application to canopy reflectance modeling: The SAIL model. *Remote Sensing of Environment*, 16, 125-141.

Vincent, R.K., & Thomson, F. J. (1971). Discrimination of basic silicate rocks by recognition maps processed from aerial infrared data. *Proceedings of the Seventh International Symposium on Remote Sensing Environment*(pp. 245-251). Ann Arbor, MI: University of Michigan.

Warner, T. (1999). Analysis of spatial patterns in remotely sensed data using multivariate spatial correlation. *Geocarto International,* 14: 59-65.

Warner, T. A. & Chen, X. (2001). Normalization of Landsat thermal imagery for the effects of solar heating and topography. *International Journal of Remote Sensing*, 22, 773-788.

Woodcock, C. E, Strahler, A. H., & D. L. Jupp (1988). The use of variograms in remote sensing: I. Scene models and simulated images. *Remote Sensing of Environment,* 25, 323-348.

Tables

Table 2.1. Minerals, rock types, and alteration types used to create the simulated data

Type	**Name**
Minerals	Quartz, calcite, hematite, goethite, alunite, kaolinite, montmorillonite, muscovite, gypsum.
Unaltered rocks	Basalt, limestone, sandstone, siltstone
Altered rocks	Silicified rocks, opalized rocks, and argillized rocks.

Table 2.2. Summary characteristics of the MASTER and AVIRIS instruments

Characteristic	**Sensor**	
	MASTER	**AVIRIS**
Wavelength range	0.4-13 μm	0.4-2.5 μm
Number of spectral bands	50	224
Channel width	Varies, 40 to 650 nm	10 nm
Instantaneous field of view	2.5 mrad	1 mrad
Total field of view	85.92º	33º
Number of pixels	716	614
Platform	B200, ER-2, DC-8	ER-2, Twin Otter
Digitization	16-bit	12-bit

Table 2.3. Uncertainty categories of the simulated data

Group	Simulated Noise			
	System	Solar Illumination	Mixed pixels (proportion of cover type)	
			Vegetation	Additional mineral/rock
1	X			
2	X	X		
3	X	X	0-5%	
4	X	X	0-5%	0-10%
5	X	X	0-10%	0-10%
6	X	X	0-10%	0-20%
7	X	X	0-10%	0-30%

Table 2.4. Classification accuracies of data set 7 minerals and rocks using SAM and SFF

Mineral or rock	Accuracy: SAM				Accuracy: SFF			
	AVIRIS		COMBINED		AVIRIS		COMBINED	
	Prod.	User	Prod.	User	Prod.	User	Prod.	User
Alunite	96.5	90.7	97.1	95.7	100.0	83.4	94.1	100.0
Basalt	68.4	100.0	47.8	87.2	85.6	90.0	80.8	91.7
Calcite	92.8	72.7	97.1	89.7	100.0	38.6	99.9	46.7
Goethite	83.0	73.9	91.2	92.5	99.1	97.0	89.3	96.0
Hematite	89.2	96.3	99.1	98.4	98.8	98.0	96.4	99.5
Kaolinite	98.9	87.2	99.0	97.3	99.9	77.4	79.5	100.0
Montmorillonite	94.2	69.8	95.5	90.9	99.7	94.3	81.0	100.0
Muscovite	80.0	64.4	95.3	93.1	40.5	91.0	91.9	77.5
Quartz	84.2	95.7	97.8	100.0	24.0	18.5	99.9	100.0
Argillized	99.6	95.7	100.0	98.0	98.9	90.8	91.7	98.5
Limestone	24.0	42.4	71.8	63.3	22.5	58.6	82.1	93.9
Opalized	91.5	94.3	95.9	100.0	96.8	99.9	80.3	99.0
Sandstone	75.6	96.3	67.2	76.5	83.0	98.8	77.5	100.0
Siltstone	65.0	76.9	87.6	64.4	47.9	89.0	83.5	71.4
Silicified	36.1	54.0	93.9	91.5	40.6	99.1	82.0	92.3
Gypsum	89.8	100.0	90.0	100.0	99.5	100.0	90.7	100.0

Table 2.5. Classification accuracies of 9 minerals and rock on data set 7 using SFF

Mineral or rock	SWIR Band Only		VNIR and SWIR Bands	
	Prod. Acc.	User Acc.	Prod. Acc.	User Acc.
Alunite	99.8	100.0	100.0	99.0
Calcite	100.0	100.0	100.0	96.0
Goethite	0.0	0.0	99.1	99.2
Hematite	0.0	0.0	98.9	100.0
Kaolinite	99.8	98.6	100.0	99.4
Montmorillonite.	100.0	100.0	99.7	100.0
Argillized	98.0	100.0	98.9	99.7
Opalized	98.6	99.7	97.0	100.0
Gypsum	100.0	98.4	99.5	100.0

Figures

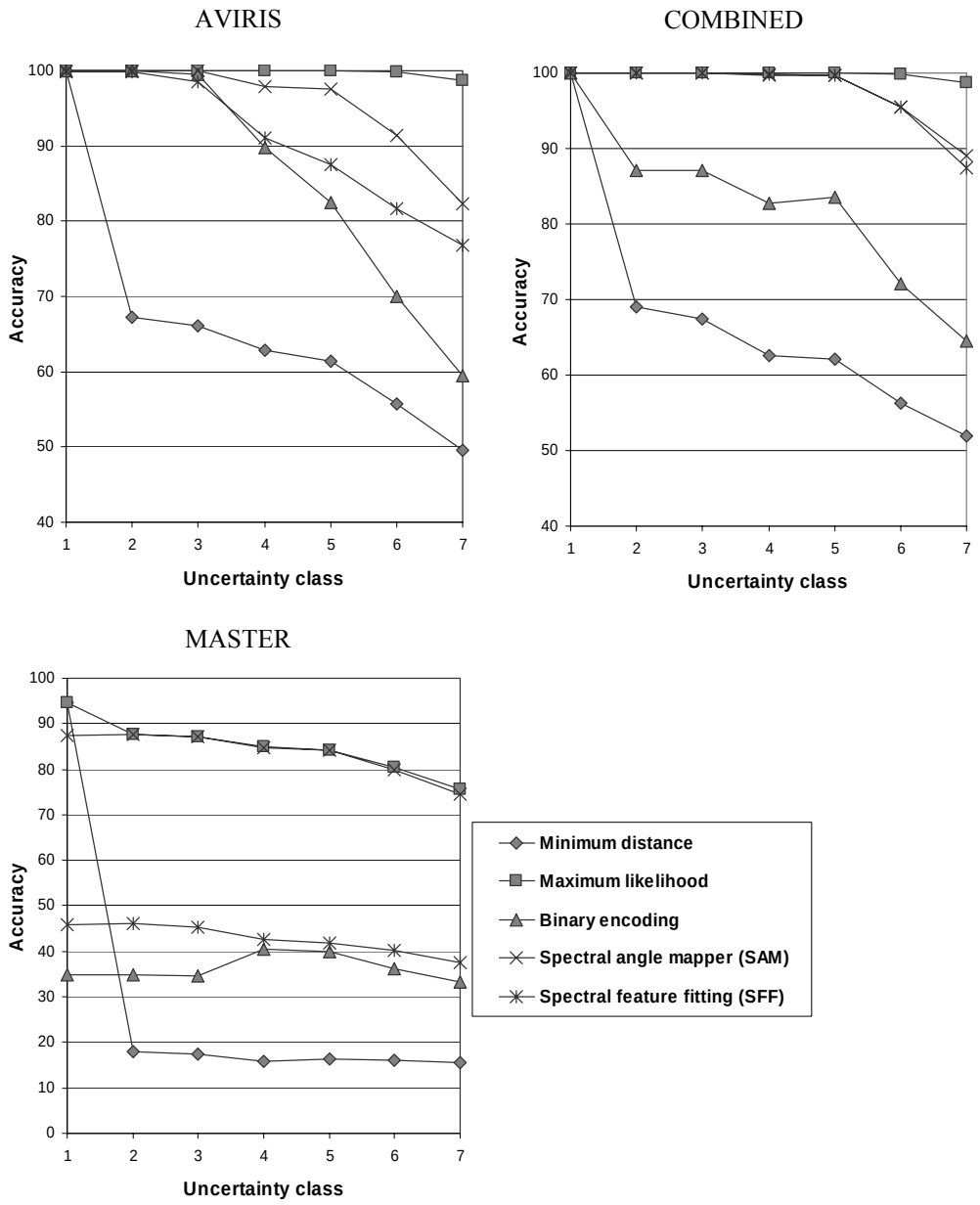

Figure 2.1. Comparison of the overall accuracies using five mapping methods on different noise categories of 16 mineral and rock classes. Upper left: AVIRIS data sets. Upper right: Combined data sets. Bottom: MASTER data sets (See Table 2.3 for description of uncertainty classes).

Figure 2.2. Overall classification accuracies of minimum distance classification and binary encoding applied to MNF transformed data sets (Uncertainty levels 5, 6, and 7).

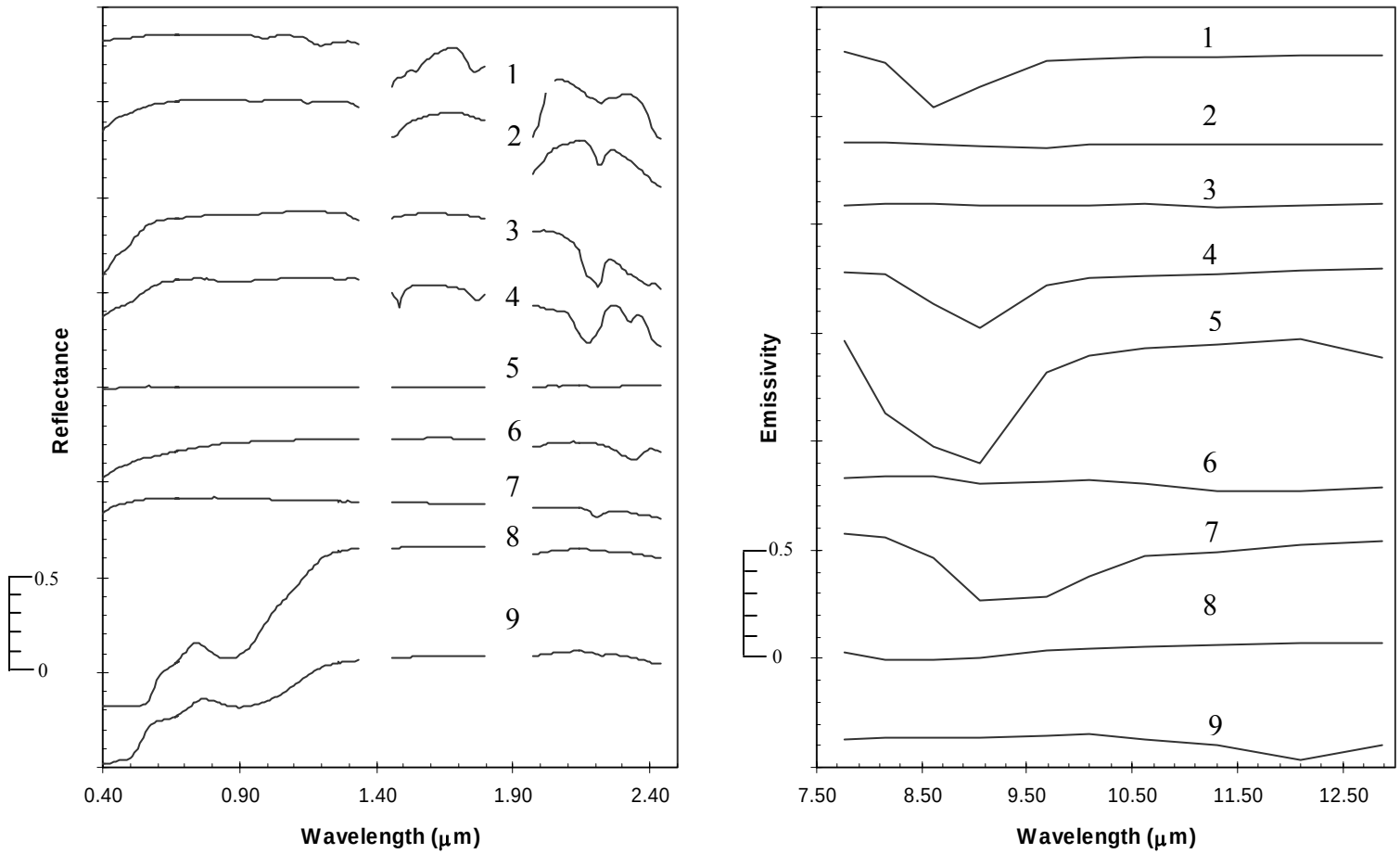

Figure 2.3. Laboratory reflectance spectra and emissivity spectra of minerals resampled to AVIRIS (left) and MASTER (right) wavelength bands. 1. Gypsum, 2. Montmorillonite, 3. Kaolinite, 4. Alunite, 5. Quartz, 6. Calcite, 7. Muscovite, 8. Hematite, 9. Goethite (Source: Spectra resampled from Salisbury *et al*., 1991, Research System 2004)

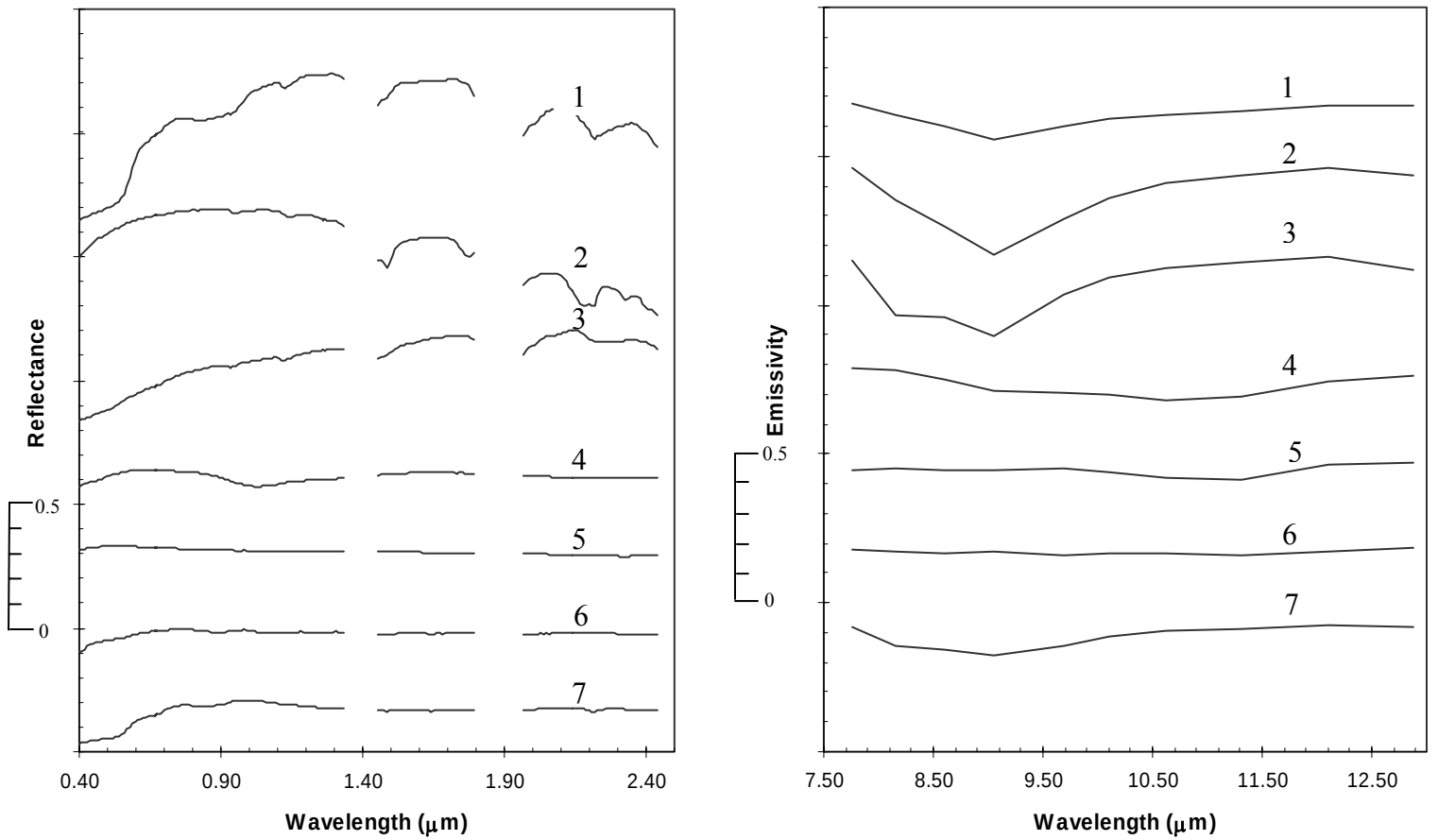

Figure 2.4. Laboratory reflectance spectra and emissivity spectra of rocks resampled to AVIRIS (left) and MASTER (right) wavelength bands. 1. Argillized, 2. Opalized, 3. Silicified, 4. Basalt, 5. Limestone, 6. Siltstone, 7. Sandstone (Source: Spectra 1-3 resampled from laboratory and field spectra acquired for this study, Spectra 4-7 resampled from Salisbury *et al*., 1991, Research System 2004)

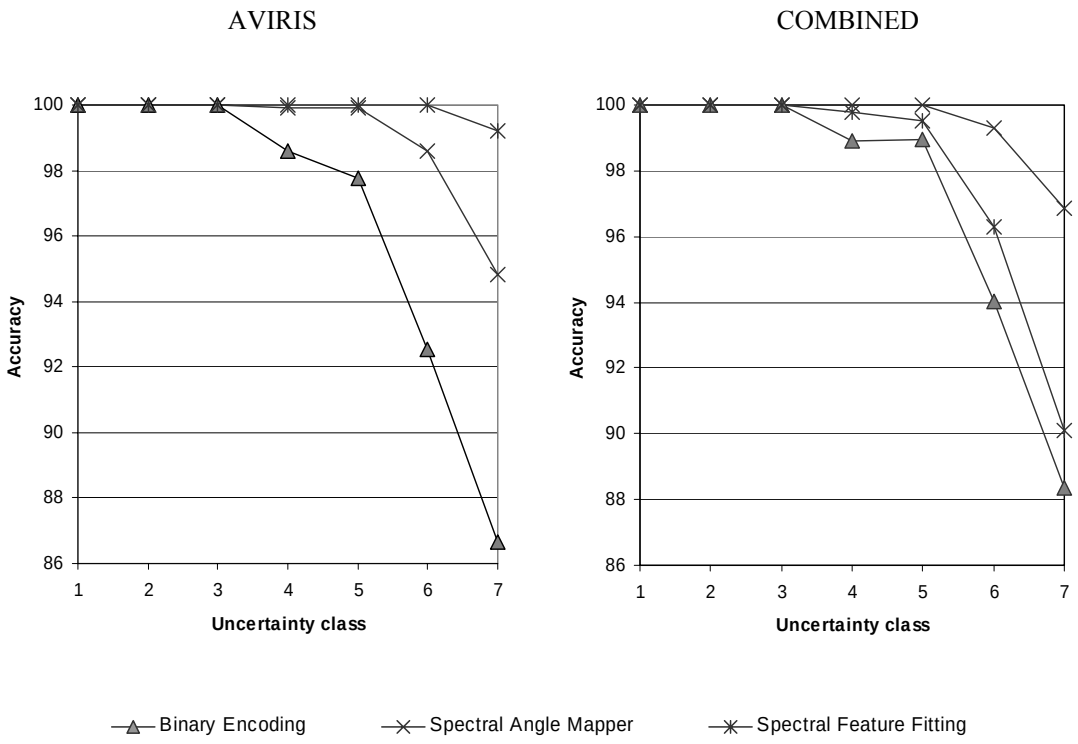

Figure 2.5. Comparison of the overall accuracies using SAM, SFF, and binary encoding on different noise categories of 9 mineral and rock classes with distinctive absorption features. Left: AVIRIS data sets. Right: Combined data sets.

Chapter 3. Real Data Analysis

Abstract

This study investigated the potential value of integrating hyperspectral visible, near infrared, and short wave infrared imagery with multispectral thermal data for geological mapping. Two coregistered aerial data sets of Cuprite, Nevada were used: Airborne Visible/Infrared Imaging Spectrometer (AVIRIS) hyperspectral data, and MODIS/ASTER Airborne Simulator (MASTER) multispectral thermal data. Four classification methods were each applied to AVIRIS, MASTER, and a combined set. Confusion matrices were used to assess the classification accuracy. The assessment showed, in terms of kappa coefficient, that most classification methods applied to the combined data achieved a marked improvement compared to the results using either AVIRIS or MASTER TIR data alone. SAM showed the best overall classification performance. Minimum distance classification had the second best accuracy, followed by SFF and maximum classification. The results of the study showed that SFF applied to the combination of AVIRIS with MASTER TIR data are especially valuable for identification of silicified alteration and quartzite sandstone, both of which exhibit distinctive features in the TIR region. SAM showed some advantages over SFF in dealing with multispectral TIR data, obtaining higher accuracy in discriminating low albedo volcanic rocks and limestone which do not have unique, distinguishing features in the TIR region.

Key Words: hyperspectral; multispectral; thermal; classification methods; MASTER; AVIRIS; data integration.

1. Introduction

The potential for lithologic mapping with hyperspectral data from the reflected solar spectrum has been demonstrated since the first acquisition by the Airborne Imaging Spectrometer (AIS) in 1983. Imaging spectrometers measure radiance in many contiguous narrow bands, typically from the visible and near-infrared (VNIR, 0.4 - 1.1 μm), as well as short-wavelength infrared (SWIR, 1.1 - 2.5 μm). The spectral bandwidths of hyperspectral image bands are generally less than 25 nm, in order to facilitate the identification of spectral absorption features that are often diagnostic of specific minerals (Clark, 1999). For example, hydroxyl-bearing minerals and carbonate minerals can potentially be discriminated by identifying characteristic spectral features in the 0.4 - 2.5 μm region. However some silicate minerals or silicate bearing rocks such as quartz and basalt do not exhibit diagnostic absorption features in VNIR and SWIR regions. It is difficult to accurately identify these minerals or rocks using VNIR and SWIR hyperspectral data.

Complementing the development of hyperspectral remote sensing has been the development of multispectral thermal infrared (TIR, 8-12 μm) instruments, which measure TIR radiance in a small number of broad bands. Multispectral TIR radiance contains information regarding both the temperature and emissivity of the radiating surface, with the effect of temperature generally dominating the spectra (Hook *et al.*, 1992). The separation of surface temperature and emissivity is complex because of the nonlinearity of the relationship between radiance and surface temperature, and the underdetermined nature of the problem (Hook, *et al*., 1992). A variety of techniques that approximate the separation of the emissivity from the temperature information have been

proposed (Becker and Li, 1990; Hook *et al*., 1992; Kahle *et al.*, 1980; Hook and Kahle, 1990; Kealy and Gabell, 1990; Matsunaga, 1994; Gillespie *et al*., 1998). The derived emissivity spectra usually have relative high uncertainties and low contrasts. These properties, in addition to the broad spectral bands that may not be sufficient to resolve important spectral features, limit accurate classification of surface composition using spectral analysis methods with only multispectral TIR data (Collins, 1991).

Emissivity spectra nevertheless do have potential for discriminating rocks and minerals, especially silicates and oxides (Collins, 1991; Hook *et al*., 1994; Rowan and Mars, 2003; Sabine *et al*., 1994). The emissivity spectral features of silicates and oxides relate to Si-O bonding, ion mass, and crystal structure. In particular, the emissivity spectra minimum of silicates shifts to progressively shorter wavelength as the Si-O bond strength increase (Vincent and Thomson, 1967; Hunt and Salisbury 1974).

Thus, the information provided by multispectral TIR tends to be complementary to that of the VNIR and SWIR regions (Hook *et al.,* 1999). Very little attention, however, has been paid to image analysis approaches that simultaneously draw on both VNIR/SWIR hyperspectral and TIR multispectral data. One early exception is Abram and Hook (1991), who pointed out that combining AVIRIS (Airborne Visible/Infrared Imaging Spectrometer) and TIMS (Thermal Infrared Multispectral Scanner) data might assist the classification of silicified alteration and limestone.

Chapter 2 showed that integrating VNIR/SWIR hyperspectral with TIR multispectral data could potentially result in a large improvement in the identification of oxide and silicate minerals, at least with simulated data. In this chapter, real AVIRIS and MASTER (MODIS/ASTER Airborne Simulator) TIR data sets of Cuprite, Nevada, are

used to investigate whether integrating VNIR/SWIR hyperspectral analysis with TIR multispectral analysis will indeed provide improved lithologic mapping.

2. Classification algorithms

The relative information of singular and combined AVIRIS and MASTER data was evaluated using four image classification methods. Using a range of classification methods is useful, because the relative accuracy of combining disparate wavelength regions may vary with the type of method used. The methods selected include two statistical classification methods, minimum distance and maximum likelihood classification, and two spectral analysis approaches, spectral feature fitting (SFF) and the spectral angle mapper (SAM). Each of these methods is described briefly below.

Minimum distance classification compares Euclidean distances calculated for an unknown pixel to each class mean vector, which is estimated from the training data. The unknown pixel is assigned to the class with nearest mean vector. Minimum distance classification is attractive because it requires only a simple calculation and a relatively small number of training samples (Richards, 1993).

Maximum likelihood classification is one of the most common supervised classification methods. Training data are used to calculate the class mean vector and covariance matrix, which in turn is used to estimate the class probability distribution function. An unknown pixel is assigned to the class with which it has the largest membership likelihood, as determined from the probability density functions. The effectiveness of maximum likelihood classification depends upon acquiring sufficient training data to allow reasonably accurate estimation of the class statistics (Richards,

1993). It has been suggested that the minimum number of training samples must be ten times to 100 times the number of bands (Swain and Davis, 1978).

Spectral feature fitting (SFF) (Crowley *et al.,* 1989; Clark *et al.,* 1990) is based on a comparison of the absorption features in the image and reference spectra. The first step in SFF is the enhancement of absorption features using the continuum removal algorithm. The continuum is defined as a convex hull fit over the top of each spectrum utilizing straight line-segments to connect local spectrum maxima (Clark *et al*., 2003, Kruse *et al.,* 1993b), and is removed by dividing the convex hull into the original spectrum. The second step is the calculation of a least-square estimate of the goodness of fit between the continuum removed pixel spectrum and reference spectra. SFF has an advantage over other methods in that it minimizes the influences of the effect of mixtures of materials, the mineral grain sizes, and the illumination for that pixel.

Spectral angle mapper (SAM) (Kruse *et al*., 1993a) is a fast and efficient spectral analysis algorithm for calculating the similarity between pixel spectra and reference spectra in terms of the angle between two *n*-dimensional vectors, where *n* is the number of bands of hyperspectral data. One of the advantages of SAM is that it tends to normalize for variation in topographic illumination effects (Pouch and Campagna, 1990).

3. Geologic setting of study area

Cuprite, Nevada, is an ideal geologic test site because a wide variety of rock types and alteration types are exposed, with only sparse vegetation cover. In addition, the topographic relief is relatively low. Furthermore, because Cuprite has been used as a test site for more than two decades, a wide range of previous studies is available for comparison (Abrams *et al*., 1977a; Abrams *et al*., 1977b; Abrams and Ashley, 1980;

Goetz and Srivastava, 1985; Abrams and Hook, 1991; Kruse *et al*., 1990; Hook *et al*., 1992; Van der Meer and Bakker, 1997).

Cuprite is located on the western edge of Esmeralda County, Nevada (37° 29′ to 37° 35′ North, 117° 9′ to 117° 17′ West) and is separated into east and west sections by US Highway 95 (Figure 3.1). The east section is dominated by Tertiary volcanic rocks and Quaternary alluvial deposits. Cambrian sedimentary rocks, Tertiary volcanics, and Quaternary alluvial deposits are exposed in the west section. The Cambrian sedimentary rocks include sandstone, siltstone, and limestone. The Tertiary volcanic rocks consist of ash-flow and air-fall tuff, conglomerate, and basalt (Ashley, 1974; Abrams *et al*., 1977a; Abrams *et al*., 1977b).

Three field mappable zones of hydrothermal alteration related to fossilized hot springs have been identified at Cuprite: silicified rocks, opalized rocks, and argillized rocks. Abundant quartz, some calcite, and minor alunite and kaolinite are present in the silicified zone, which comprises the most intensely altered rocks in the study area. The opalized zone, the most widespread alteration zone, contains opal and variable amount of alunite and kaolinite. The argillized zone comprises the least intensely altered rocks, and generally separates the country rock from the opalized rocks. The dominant minerals of the argillized zone include opal, kaolinite, and montmorillonite. In addition to the minerals mentioned above, small amounts of hematite are present in the opalized and argillized rocks (Abrams and Ashely, 1980).

4. Data sets

The Airborne Visible/Infrared Imaging Spectrometer (AVIRIS) data

The Airborne Visible/Infrared Imaging Spectrometer (AVIRIS) (Green *et al*., 1998) has been flown by NASA since 1987. AVIRIS acquires data in 224 narrow, contiguous spectral bands across the reflected solar energy region (0.4-2.5 μm) (Table 3.1). AVIRIS is regarded as one of the premiere hyperspectral instruments because of its high signal-noise ratio (SNR) and good image geometry. The AVIRIS data of Cuprite (Figure 3.1, left) was acquired on June 19, 1996, at a flying height of 20 km, with approximately 20 m pixels.

MODIS/ASTER Airborne Simulator (MASTER)

The MODIS/ASTER Airborne Simulator (MASTER) was developed to support scientific studies prior to the launch of the Advanced Spaceborne Thermal Emission and Reflection Radiometer (ASTER) and the Moderate Resolution Imaging Spectroradiometer (MODIS) (Hook *et al*., 2001). The MASTER instrument (Table 3.1) has 10 TIR bands of which a total of 50 bands cover the 0.4-13 μm wavelength region. The MASTER data that are used in this study (Figure 3.1, right) were acquired at approximately 19:36 GMT on June 9, 1999, under clear weather conditions. The instrument flown on a US Department of Energy King Air B-200, at elevation of 9,648 meters above the ground, resulting in approximately 20 m pixels.

5. Data preprocessing methods and analysis

5.1 Image preprocessing

Prior to the spectral analysis of the AVIRIS and MASTER data, a range of pre-processing steps was applied, including image rectification and calibration of radiance to reflectance or emissivity.

United States Geological Survey (USGS) black and white Digital Orthophoto Quarter Quadrangles (DOQQs), with 1 meter pixels, were used for map control for image rectification. A total of 92 and 239 ground control points (GCPs) were identified on the DOQQs for the AVIRIS and MASTER images, respectively. A second-order polynomial transformation was performed for the AVIRIS GCPs, giving a root mean square (RMS) error of 0.72 pixels. The MASTER imagery has a more complex geometry, partly because it was acquired at a lower height than the AVIRIS data was. Consequently a rubber sheeting transformation was used to rectify the MASTER data, with a RMS error of 0.89 pixels based on 30 evaluation points. Both images were resampled to the same UTM grid, using nearest neighbor convolution.

The main atmospheric effects on TIR radiance include atmospheric absorption, downwelling atmospheric irradiance, and upwelling atmospheric path radiance. The MODTRAN4 atmospheric model (Berk *et al.*, 1999), implemented as PCModWin (Ontar Corporation, 2002), was used to estimate these three atmospheric parameters for the MASTER data. Ignoring the incident radiance from adjacent pixels, the TIR at-sensor radiance is expressed by following equation (Gillespie *et al*., 1998):

$$L_{x,y,\lambda} \approx \tau_{x,y,\lambda}\ \varepsilon_{x,y,\lambda}\ B_{\lambda}(T_{x,y}) + \tau_{x,y,\lambda}\ \rho_{x,y,\lambda}\ S{\downarrow}_{x,y,\lambda} + S{\uparrow}_{y,x,\lambda} \quad (1)$$

Where

x, y = position in scene (m)

λ = wavelength

L = radiance at-sensor (Wm^{-2} μm^{-1} sr^{-1})

B = radiance of black body at temperature T (Wm^{-2} μm^{-1} sr^{-1})

T = temperature (Kevin)

ε = emissivity of ground surface

$S\downarrow$ = downwelling atmospheric irradiance, normalized by π sr (Wm^{-2} μm^{-1} sr^{-1})

τ = atmospheric transmissivity

ρ = reflectance of ground surface

$S\uparrow$ = upwelling atmospheric path radiance (Wm^{-2} μm^{-1} sr^{-1})

Airsonde data acquired at the time of over-flight was used for the atmospheric profile to estimate $S\downarrow$, $S\uparrow$, and τ. Surface radiance data of TIR was retrieved from Equation 1, and subsequently converted to estimated emissivity using the ENVI implementation of the alpha residual method (Hook, *et al.*, 1992). The alpha residual method was chosen because it is relatively straightforward to calculate, yet is less susceptible to noise than the reference channel and emissivity normalization technique (Kealy and Hook, 1993).

All bands near the atmospheric water absorption regions of 1.4, 1.9, 2.5, 7.7, 12.8 μm, as well as some bands with relative low signal-noise ratio (AVIRIS bands 1-3) were deleted, leaving a total of 185 out of the 224 AVIRIS bands, and 8 out of 10 TIR MASTER bands for the analysis.

5.2 Lithologic classes

A total of 11 lithological classes, including volcanic tuffs, basalt, diabase, felsite dyke, limestone, siltstone, sandstone, argillized rocks, opalized rocks, and silicified rocks, were chosen for the spectral classification. All classification and spectral analysis methods were carried out with ENVI image analysis software (Research System, 2004). Regions from which the training data for the classification were selected were chosen based on Abrams and Ashley's (1980) geological and alteration map of Cuprite, as well as field work by the authors, conducted in 2004. The geological map is relatively generalized, categorizing lower Cambrian sandstone and siltstone into a single lithologic unit, the Harkless Formation (Abrams and Ashley, 1980). However, it was found through field work and preliminary visual interpretation that these two rock types could be differentiated based on their spectral characteristics. In addition, an additional lithologic class, diabase, which was not shown on the geological map, was identified in the field work.

5.3 Classification accuracy assessment

To investigate the potential value of integration of VNIR/SWIR hyperspectral analysis with TIR multispectral analysis, the accuracies of classification results using the AVIRIS, MASTER, and combined data were compared. The classification accuracy was summarized using a confusion, or contingency, matrix. The test data were independent of the training data, but were also selected based on the geological map and field work.

To compare the two classification results, the Kappa coefficient, a measure of how well the predicted rock units agree with the test data, was computed for each matrix. The Kappa coefficient is calculated by

$$K = \frac{N\sum_{k} X_{kk} - \sum_{k} X_{k\Sigma} X_{\Sigma k}}{N^2 - \sum_{k} X_{k\Sigma} X_{\Sigma k}} \qquad (2)$$

where N is the total number of pixels in all the testing samples, $\sum_{k} X_{kk}$ is the sum of the confusion matrix diagonals (X_{kk}), $X_{k\Sigma}$ is the sum of the testing samples in class k, $X_{\Sigma k}$ is the sum of the predicted pixels in class k (Cohen, 1960, Research Systems, 2004). The overall accuracy, computed by summing the number of pixels predicted correctly and dividing by the total number of testing samples, is another parameter indicating the overall agreement. The producer's accuracy is the probability that a pixel is predicted as class A, given that the ground truth class is indeed A. User's accuracy is the probability that true class is A given a pixel is predicted as class A. The producer's and user's accuracies are measures of how well each individual class is classified.

6. Results

Kappa coefficients of classification using training samples selected from the imagery showed that for SAM, minimum distance, maximum likelihood classification, the overall accuracy was notably greater with the combined data set, than with the AVIRIS or MASTER data alone (Figure 3.2). SAM applied to the combined data set achieved the highest accuracy, followed by minimum distance classification, SFF and maximum likelihood classification. The results of classifications of the AVIRIS data alone showed a different accuracy rank compared to classification of the combined data set. SFF obtained the highest classification accuracy, followed by maximum likelihood classification, and then SAM; minimum distance classification had the lowest accuracy. Applied to MASTER data, maximum likelihood classification had the best performance,

SAM had the second place, followed by minimum distance classification; SFF produced a relative poor result with the MASTER data. The observation that SFF was less suitable for the broad MASTER TIR bands supported the modeling results described in Chapter 2.

Although the overall accuracy of classification of SFF applied to the combined data set was slightly lower than for the AVIRIS data, some rock types showed remarkable improvement in producer accuracy's and user's accuracy (Table 3.2). For instance, basalt showed 26 percent and 47 percent increase in producer's and user's accuracy, respectively. Silicified rock and sandstone also achieved marked increase in producer's accuracy. On the other hand, limestone, opalized rock, and argillized rocks showed a large decrease in accuracy, and other rocks, such as unaltered tuff, siltstone, and felsite, showed a small decrease in accuracy.

Examining the confusion matrices of SFF (Tables 2.3 and 2.4) in more detail indicates that the worst omission error and commission error with the AVIRIS data occurred with basalt, whereas the worst omission error and commission error with the combined data set was for argillized rock. For the classification of the AVIRIS data, most of the basalt pixels were misclassified as volcanic tuff 1 and tuff 2. Neither basalt nor tuff have distinctive absorption features in the 0.4 – 2.5 μm wavelength region (Figure 3.3, left), and thus it is very difficult to discriminate these rocks in the VNIR and SWIR regions. However, in the TIR region, they exhibit Si-O features around 10 μm (Figure 3.3, right). Argillized and opalized rocks were also often confused for SFF applied to the combined data set because they have similar spectral features in the TIR region. When SFF was applied to the AVIRIS data, opalized and argillized rocks resulted in fairly high classification accuracies, even though both contain the same clay

mineral, kaolinite. Opalized rock exhibits characteristic absorption features at 1.16, 1.27, 1.72, 2.18, and 2.32 μm (Figure 3.3, right). Argillized rock has absorption features at 0.88, 2.20, and 2.32 μm.

The combination of AVIRIS with MASTER did not assist in discrimination of argillized and opalized rocks. Likewise, limestone exhibits such weak spectral feature at 9.6 and 11.3 μm region that SFF is apparently not sensitive enough to capture them. The main constituent mineral of silicified rock and sandstone is quartz, which exhibits strong Si-O feature at 9 μm position (Figure 3.3, right). Therefore, SFF with the combined AVIRIS and MASTER data is only helpful for identification of rocks which exhibit distinctive spectral features.

Table 3.5 shows that most rocks, except for opalized and argillized rocks, resulted in some improvement in classification accuracy with the SAM classification for the combined data, compared to AVIRIS alone. Silicified rock, the two volcanic tuffs, basalt, diabase, and limestone all greatly increased in classification accuracy. In particular, the classification method and data set that produced the highest accuracy for volcanic tuffs and basalt was SAM applied to the combined data set (Table 3.7). These rocks were otherwise only poorly separable (Table 3.6), probably because of a generally low albedo without distinctive absorption features in the VNIR and SWIR regions. The improvement in accuracy for silicified rocks with the combined data set applied to SAM is most likely due to the strong TIR silica feature. Limestone has only very weak features in TIR region. Nevertheless, limestone resulted in the highest accuracy among all rock types with the combined data set. These results suggest that SAM applied to the AVIRIS and MASTER TIR data has great potential for identification of a wide range of rocks and

minerals, including both those that exhibit distinctive absorption features, and those that do not.

As was found from an early modeling study (Chen *et al*., 2004), the results of SAM and SFF methods showed a relative high classification performance. However, it was surprising that minimum distance classification was the second best method when applied to the combined data. Rocks with low albedo in the VNIR and SWIR regions, such as volcanic tuffs, basalt, and diabase in particular, showed a great improvement in classification accuracy when the combined data was used with minimum distance classification. Adding TIR wavelength data for these rocks was helpful in differentiating the mean vector of these classes. The results of maximum likelihood classification indicated that its performance was highly dependent on the spectral variability of the classes. For instance, limestone, siltstone, and sandstone are relatively uniform in spectral properties in the imagery. The large areas of rock outcrops of these units were classified with a high degree of accuracy. In comparison, the felsite and argillized rocks showed much greater variability, and a very low classification accuracy.

7. Conclusions

The result of this study demonstrated the potential value of integrating hyperspectral AVIRIS data with multispectral MASTER TIR data for geological mapping. The assessment showed, in term of kappa coefficient, most classification methods applied to the combined data achieved a marked improvement compared to the results of the use of AVIRIS and MASTER TIR data alone. SAM showed the best classification performance. Minimum distance classification had the second best accuracy, followed by SFF and maximum classification. However, prior knowledge

about the study area is required in order to select training samples for performing conventional classification methods. Hyperspectral analysis methods have an advantage over maximum likelihood classification and minimum distance classification in that, at least potentially, field and library spectra can replace in-scene training data. However, for this study, the field spectra were apparently not sufficiently representative, and the resulting classification accuracies were very low.

The results of the study showed that SFF applied to the combination of AVIRIS with MASTER TIR data are especially valuable for identification of silicified alteration and quartzite sandstone which exhibit strong distinctive absorption features in the TIR region. SAM showed some advantages over SFF in dealing with multiple broad band TIR data, obtaining higher accuracy in discriminating low albedo volcanic rocks and limestone which do not have strong characteristic features in the TIR region.

Acknowledgements

The authors would like to thank Dr. S. J. Hook and Ron Alley for providing us with an atmospheric profile acquired at the time of over-flight, and Cindy Grove of the Jet Propulsion Laboratory for measuring the spectra of field collected samples. Support for this research was provided by West Virginia View.

References

Abrams, M. J. and R. P. Ashley, 1980. Alteration mapping using multispectral images – Cuprite Mining District, Esmeralda County, Nevada. *U. S. Geological Survey Open File Report* 80-367.

Abrams, M. J., R. P. Ashley, L. C. Rowan, A. F. H. Goetz, and A. B. Kahle, 1977a. Use of imaging in the 0.46-2.36 μm spectral region for alteration mapping in the Cuprite mining district, Nevada. *U. S. Geological Survey Open-File Report* 77-585, pp.18.

Abrams, M. J., R. P. Ashley, L. C. Rowan, A. F. H. Goetz, and A. B. Kahle, 1977b. Mapping of hydrothermal alteration in the Cuprite mining district, Nevada, using aircraft scanner imagery for the 0.46-2.36 μm spectral region. *Geology* 5:713-718.

Abrams, M. J. and S. J. Hook, 1991. Combined use of TIMS and AVIRIS for alteration mapping: In *Proceedings of the third Thermal Infrared Multispectral Scanner (TIMS) Workshop*, JPL Publication 91-29, 54-64.

Ashley, R. P., 1974. Goldfield mining district. In: *Guidebook to the geology of four Tertiary volcanic centers in central Nevada*. Nevada Bureau of Mines and Geology Report 19:49-66.

Becker, F. and Z. L. Li, 1990. Temperature-independent spectral indices in thermal infrared bands. *Remote Sensing of Environment* 32: 17-33.

Berk , A., G. P. Anderson, P. K. Acharya , J. H. Chetwynd , M. L. Hoke , L. S. Bernstein, E.P. Shettle , M. W. Matthew , and S. M. Adler-Golden, 1999. *MODTRAN4 Version 2 User's Manual.* Air Force Research Laboratory, Space Vehicles Directorate, Air Force Materiel Command Hanscom AFB, MA.

Chen, X., Warner, T. A., and Campagna, D. J., 2004. Integrating visible, near infrared and short wave infrared hyperspectral and multispectral thermal imagery for

geologic mapping: Simulated data, in: *Proceedings of 2004 AVIRIS Workshop***,** JPL, Pasadena, CA, March 31 – April 2, 2004.

Clark, R. N., 1999. Spectroscopy of rocks and minerals, and principles of spectroscopy. In: A. N. Rencz (Ed.), *Remote Sensing for the Earth Sciences: Manual of Remote Sensing,* 3 ed, Vol. 3, Chapter 1: 3-58, John Wiley and Sons, New York.

Clark, R. N., A. J. Gallagher, and G. A. Swayze, 1990. Material absorption band depth mapping of imaging spectrometer data using the complete band shape least-squares algorithm simultaneously fit to multiple spectral features from multiple materials. *Proceedings of the Third Airborne Visible/Infrared Imaging Spectrometer (AVIRIS) Workshop*, JPL Publication 90-54, pp 176-186.

Clark, R. N., Swayze, G. A., Livo, K. E., Kokaly, R. F., Sutley, S. J., Dalton, J. B., McDougal, R. R., & Gent, C. A. (2003). Imaging Spectroscopy: earth and planetary remote sensing with the USGS Tetracorder and expert systems. *Journal of Geophysical research* 108 (E12), 5131, doi:10.1029/2002JE001847.

Cohen, J., 1960. A coefficient of agreement for nominal scales. *Educational and Psychological Measurement* XX:37-44.

Collins, A.H.,1991. Thermal infrared spectra and images of altered volcanic rocks in the Virginia Range, Nevada. *International Journal of Remote Sensing* 12(7): 1559-1574.

Crowley, J. K., D. W. Brickey, and L. C. Rowan, 1989. Airborne imaging spectrometer data of the Ruby Mountains, Montana: mineral discrimination using relative absorption band-depth images. *Remote Sensing of Environment* 29: 121-134.

Gillespie, A.R., S. Rokugawa, T. Matsunaga, J. S. Cothern, S. Hook, and A. B. Kahle, 1998. A temperature and emissivity separation algorithm for advanced spaceborne thermal emission and reflection radiometer (ASTER) images. *IEEE Transactions on Geoscience and Remote Sensing* 36(4): 1113-1126.

Goetz, A. F. H. and V. Srivastava, 1985a. Mineralogic mapping in the Cuprite Mining District. *Proceedings of the First Airborne Imaging Spectrometer Workshop*. Jet Propulsion Laboratory, Pasadena, California, pp. 22-31.

Goetz, A. F. H., G. Vane, J. E. Solomon, and B. N. Rock, 1985b. Imaging spectrometry for earth remote sensing. *Science*, 211: 1147-1153.

Green, R. O., M. L. Eastwood, C. M. Sarture, T. G. Chrien, M. Aronsson, B. J. Chippedale, J. A. Faust, B. E. Pavri, C. J. Chovit, M. Solis, M. R. Olah, and O. Williams, 1998. Imaging Spectroscopy and the Airborne Visible/Infrared Imaging Spectraometer (AVIRIS). *Remote Sensing of Environment* 65:227-248.

Hook, S. J. and A. B. Kahle, 1990. Techniques for the extraction of emissivity from multispectral thermal infrared data. *Proceeding of the International Geoscience and Remote Sensing Symposium* (IGARSS'90). College Park, Maryland. U. S. A., pp. 983-990.

Hook, S. J., E. A. Abbott, C. Grove, A. B. Kahle, and F. Palluconi, 1999. Use of multispectral thermal infrared data in geological studies. In: A. N. Rencz (Ed.), *Remote Sensing for the Earth Sciences*: Manual of Remote Sensing, 3 ed, Vol. 3, Chapter 2: 59-110, John Wiley and Sons, New York.

Hook, S. J., A. R. Gabell, A. A. Green, and P. S. Kealy, 1992. A comparison of techniques for extracting emissivity information from thermal infrared data for geologic studies. *Remote Sensing of Environment* 42(2): 123-135.

Hook, S. J., K. E. Karlstrom, C. F. Miller, and K. J. W. McCaffrey, 1994. Mapping the Piute Mountains, California, with thermal infrared multispectral scanner (TIMS) images. *Journal of Geophysical Research* 99(B8): 15,605-15,622.

Hook, S. J., J. J. Myers, K. J. Thome, M. Fitzgerald, and A. B. Kahle, 2001. The MODIS/ASTER Airborne Simulator (MASTER) – a new instrument for earth science studies. *Remote Sensing of Environment* 76: 93-102.

Hunt, G.R., and J. W. Salisbury, 1974. Mid-infrared spectral behavior of igneous rocks, In *Technical Report* AFRCL-TR-75-0356, US Air Force Cambridge Research Laboratory, Cambridge, MA.

Kahle, A. B., D. P. Madura, and J. M. Soha, 1980. Middle infrared multispectral aircraft scanner data: analysis for geological applications. *Applied Optics* 191: 2279-2290.

Kealy, P. S. and A. R. Gabell, 1990. Estimation of emissivity and temperature using alpha coefficients. *Proceeding of the First JPL Airborne Geoscience Workshop*, Jet Propulsion Laboratory, Pasadena, California.

Kealy, P. S. and S. Hook, 1993. Separating temperatures and emissivity in thermal infrared multispectral scanner data: Implication for recovering land surface temperatures. *IEEE Transactions on Geoscience and Remote Sensing* 31: 1155-1164.

Kruse, F. A., A. B. Lefkoff, J. B. Boardman, K. B. Heidebrecht, A. T. Shapiro, P. J. Barloon, and A. F. H. Goetz, 1993a. The spectral image processing system (SIPS) – Interactive visualization and analysis of imaging spectrometer data. *Remote Sensing of Environment* 44: 145-163.

Kruse, F. A., A. B. Lefkoff, and J. B. Dietz, 1993b. Expert system-based mineral mapping in Northern Death Valley, California/Nevada, Using the Airborne Visible/Infrared Imaging Spectrometer (AVIRIS). *Remote Sensing of Environment* 44: 309-336.

Kruse, F. A., K. S. Kierein-Young, and J. W. Boardman, 1990. Mineral mapping at Cuprite, Nevada with a 63 channel imaging spectrometer. *Photogrammetry Engineering and Remote Sensing* 56(1): 83-92.

Matsunaga, T., 1994. A temperature-emissivity separation method using an empirical relationship between the mean, the maximum, and the minimum of the thermal infrared emissivity spectrum. Journal of the *Remote Sensing Society of Japan* 14(2): 230-241 (in Japanese with English abstract).

Ontar Corporation, 2002. *PcModWin Manual, Version 4.0 V1R1, Version 1.1.* Ontar Corporation, North Andover, MA.

Pouch, G. W. & Campagna, D. J. (1990). Hyperspherical direction cosine transformation for separation of spectral and illumination information in digital scanner data. *Photogrammetric Engineering and Remote Sensing*, 56, 475-479.

Richards, J.A, 1993. *Remote Sensing Digital Image Analysis: An Introduction*. Springer-Verlag, New York, pp. 340.

Research Systems, 2004. ENVI User's Guide, ENVI 3.6. Research Systems, Boulder CO., pp. 1050.

Rowan, L. C. and J. C. Mars, 2003. Lithologic mapping in the Mountain Pass, California area using Advanced Spaceborne Thermal Emission and Reflection Radiometer (ASTER) data. *Remote Sensing of Environment* 84: 350-366.

Sabine, C., V.J. Realmuto, and J.V. Taranik, 1994. Quantitative estimation of granitoid composition from thermal infrared multispectral scanner (TIMS) data, Desolation Wilderness, northern Sierra Nevada, California. *Journal of Geophysical Research* 99(B3): 4261-4271.

Swain, P. & Davis, S. M. (1978). *Remote Sensing: The Quantitative Approach*. (pp. 396). New York: McGraw Hill

Van der Meer, F. and W. Bakker, 1997. CCSM: Cross correlogram spectral matching. *International Journal of Remote Sensing* 18: 1197-1201.

Vincent, R.K., and F. J. Thomson, 1972. Discrimination of basic silicate rocks by recognition maps processed from aerial infrared data. *Proceedings of the Seventh*

International Symposium on Remote Sensing Environment, pp. 245-251. Ann Arbor, MI: University of Michigan.

Tables

Table 3.1. Summary characteristics of the MASTER and AVIRIS instruments

Characteristics	**Sensor**	
	MASTER	**AVIRIS**
Wavelength range	0.4-13 μm	0.4-2.5 μm
Number of channels	50	224
Channel width	Varies, 40 to 650 nm	10 nm
Instantaneous field of view	2.5 mrad	1 mrad
Total field of view	85.92º	33º
Number of pixels	716	614
Platform	B200, ER-2, DC-8	ER-2, Twin Otter
Digitization	16-bit	12-bit
Number of spectrometers	4	4

Table 3.2. Classification accuracies of rocks using SFF applied to AVIRIS, MASTER TIR, and combined data

Mineral or rock	Accuracy: SFF (%)					
	AVIRIS		MASTER		COMBINED	
	Prod.	User	Prod.	Prod.	Prod.	User
Silicified	80.7	99.1	16.2	66.7	95.3	96.1
Opalized	66.1	89.6	34.5	33.4	65.6	74.6
Argillized	75.8	68.3	54.2	24.3	60.0	36.6
Tuff 1	76.5	61.3	72.6	54.8	69.4	66.1
Tuff 2	92.8	86.5	75.4	62.5	77.1	72.7
Basalt	53.8	40.0	83.0	76.8	79.1	87.1
Diabase	61.7	58.2	6.0	28.3	33.4	95.3
Limestone	98.8	96.3	86.4	61.6	86.7	98.5
Siltstone	97.7	79.7	94.4	79.7	98.1	80.6
Sandstone	68.2	94.8	20.4	66.1	85.8	98.6
Felsite	99.2	98.3	5.9	25.2	78.3	81.4

Table 3.3. Confusion matrix for SFF applied to AVIRIS data (overall accuracy 81.0 %)

Class	Silicified	Opalized	Argillized	Tuff 1	Tuff 2	Basalt	Diabase	Limest.	Siltstone	Sandst.	Felsite	User's Accuracy (%)
Silicified	1126	10	0	0	0	0	0	0	0	0	0	99.1
Opalized	18	759	70	0	0	0	0	0	0	0	0	89.6
Argillized	0	236	508	0	0	0	0	0	0	0	0	68.3
Tuff 1	95	51	89	753	0	184	48	0	0	8	0	61.3
Tuff 2	55	12	3	47	1189	69	0	0	0	0	0	86.5
Basalt	102	0	0	184	93	304	63	14	0	0	0	40.0
Diabase	0	18	0	0	0	0	264	0	21	151	0	58.2
Limestone	0	5	0	0	0	8	21	1111	5	0	4	96.3
Siltstone	0	29	0	0	0	0	0	0	1125	256	1	79.7
Sandstone	0	17	0	0	0	0	32	0	0	891	0	94.8
Felsite	0	11	0	0	0	0	0	0	0	0	645	98.3
Prod. Acc. (%)	80.7	66.1	75.8	76.5	92.8	53.8	61.7	98.8	97.7	68.2	99.2	

Table 3.4. Confusion matrix for SFF applied to combined data (overall accuracy 79.2 %)

Class	Silicified	Opalized	Argillized	Tuff 1	Tuff 2	Basalt	Diabase	Limest.	Siltstone	Sandst.	Felsite	User's Accuracy (%)
Silicified	1330	27	91	0	0	0	0	0	0	10	8	96.1
Opalized	5	753	237	0	0	0	0	0	0	0	14	74.6
Argillized	27	319	402	3	30	5	89	0	11	115	99	36.6
Tuff 1	0	0	0	683	242	60	49	0	0	0	0	66.1
Tuff 2	0	0	0	296	988	14	10	50	0	0	2	72.7
Basalt	0	0	0	0	0	447	29	37	0	0	0	87.1
Diabase	0	0	1	1	0	4	143	0	0	0	1	95.3
Limestone	0	0	0	0	0	11	0	975	0	0	4	98.5
Siltstone	0	36	16	0	0	24	100	30	1129	53	13	80.6
Sandstone	3	12	1	0	0	0	0	0	0	1121	0	98.6
Felsite	31	1	4	1	22	0	8	31	11	7	509	81.4
Prod. Acc. (%)	95.3	65.6	60.0	69.4	77.1	79.1	33.4	86.7	98.1	85.8	78.3	

Table 3.5. Classification accuracies of rocks using SAM applied to AVIRIS, MASTER TIR, and combined data

Mineral or rock	Accuracy: SAM (%)					
	AVIRIS		MASTER		COMBINED	
	Prod.	User	Prod.	Prod.	Prod.	User
Silicified	54.4	64.5	59.2	74.0	75.4	90.4
Opalized	67.2	88.2	36.7	50.8	64.8	91.2
Argillized	84.3	60.8	49.7	26.1	90.9	52.3
Tuff 1	73.1	79.7	62.3	50.0	99.3	91.3
Tuff 2	76.9	82.9	62.7	65.6	93.8	96.3
Basalt	70.8	32.2	84.3	73.0	88.3	97.7
Diabase	57.5	65.6	41.4	34.4	85.8	86.0
Limestone	67.8	92.8	85.1	99.7	100.0	99.6
Siltstone	93.8	88.3	93.4	86.0	97.3	85.8
Sandstone	89.7	92.6	55.1	64.7	84.3	96.6
Felsite	45.4	42.0	66.6	79.6	65.4	58.1

Table 3.6. Confusion matrix for SAM applied to AVIRIS data (overall accuracy 72.4 %)

Class	Silicified	Opalized	Argillized	Tuff 1	Tuff 2	Basalt	Diabase	Limest.	Siltstone	Sandst.	Felsite	User's Accuracy (%)
Silicified	759	49	18	0	0	61	0	0	0	0	289	64.5
Opalized	10	771	84	0	0	0	0	0	0	0	9	88.2
Argillized	41	320	565	0	0	0	3	0	0	0	1	60.8
Tuff 1	71	0	0	720	99	14	0	0	0	0	0	79.7
Tuff 2	20	0	0	172	986	12	0	0	0	0	0	82.9
Basalt	163	0	0	87	197	400	23	354	5	0	15	32.2
Diabase	45	0	0	0	0	0	246	4	42	8	30	65.6
Limestone	0	0	0	0	0	59	0	763	0	0	0	92.8
Siltstone	0	1	0	0	0	0	18	0	1079	123	1	88.3
Sandstone	0	0	0	0	0	0	80	0	4	1171	10	92.6
Felsite	287	7	3	5	0	19	58	4	21	4	295	42.0
Prod. Acc. (%)	54.4	67.2	84.3	73.2	76.9	70.8	57.5	67.8	93.7	89.7	45.4	

Table 3.7. Confusion matrix for SAM applied to combined data (overall accuracy 86.2 %)

Class	Silicified	Opalized	Argillized	Tuff 1	Tuff 2	Basalt	Diabase	Limest	Siltstone	Sandst	Felsite	User's Accuracy (%)
Silicified	1053	16	1	0	0	0	0	0	0	0	95	90.4
Opalized	9	744	53	0	0	0	0	0	0	0	10	91.2
Argillized	38	386	609	4	0	0	0	0	17	0	110	52.3
Tuff 1	0	0	3	977	59	24	3	0	0	0	4	91.3
Tuff 2	0	0	0	3	1203	35	8	0	0	0	0	96.3
Basalt	0	0	0	0	0	499	12	0	0	0	0	97.7
Diabase	0	0	0	0	20	7	367	0	0	33	0	86.0
Limestone	0	0	0	0	0	0	0	1125	1	0	4	99.6
Siltstone	0	0	3	0	0	0	38	0	1120	142	2	85.8
Sandstone	35	0	0	0	0	0	0	0	0	1101	0	96.9
Felsite	261	2	1	0	0	0	0	0	13	30	425	58.1
Prod. Acc. (%)	75.4	64.8	90.9	99.3	93.8	88.3	85.8	100.0	97.3	84.3	65.4	

Figures

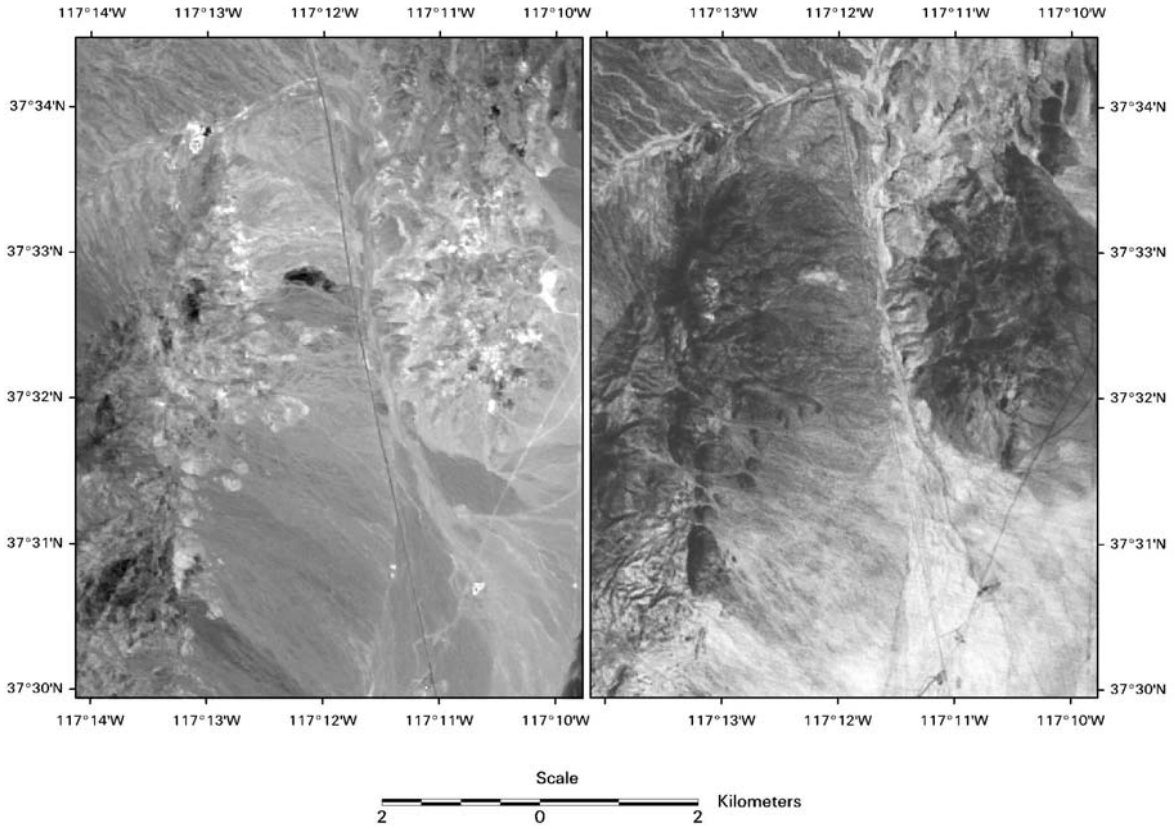

Figure 3.1. Left: AVIRIS image of Cuprite, Nevada (band 199, 2.26 μm). Right: MASTER image of the same area (band 45, 9.67 μm).

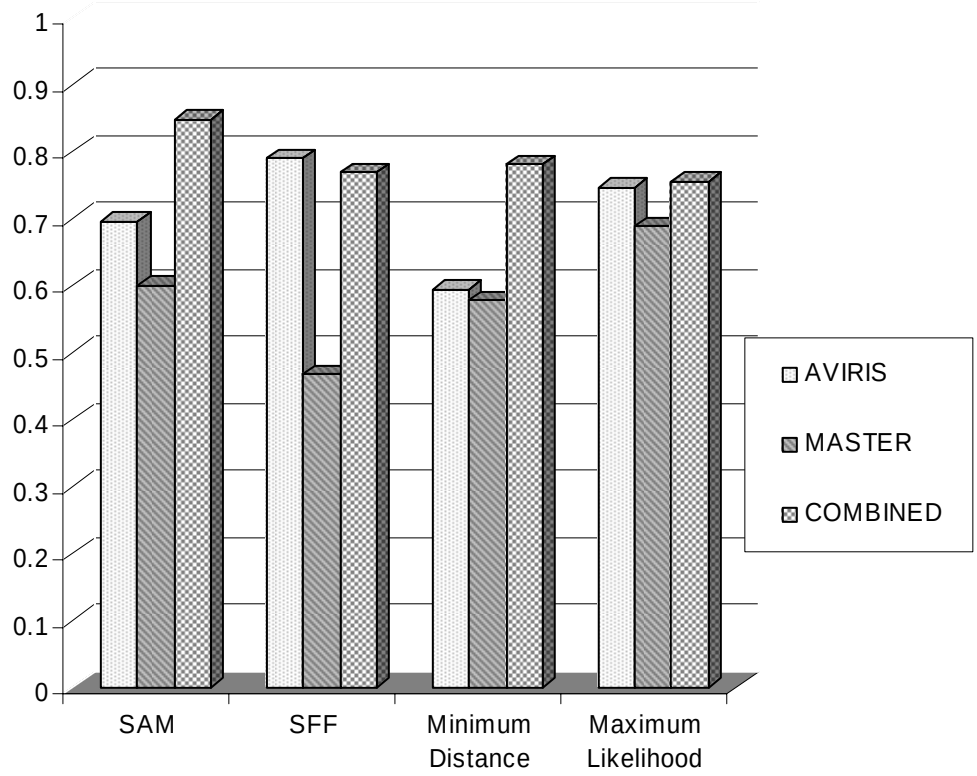

Figure 3.2. Kappa coefficients of five classification methods applied to AVIRIS, MASTER TIR, and combined data.

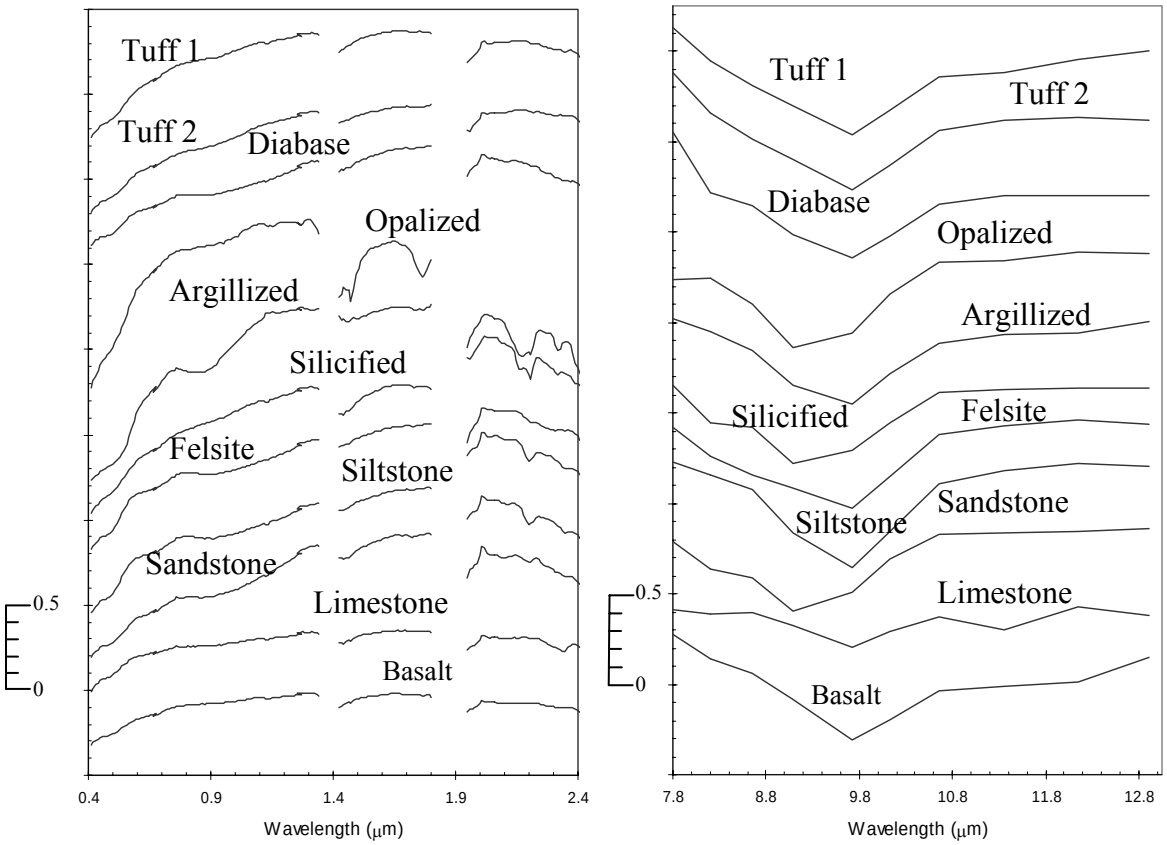

Figure 3.3. Image derived reflectance spectra and alpha emissivity residual spectra of eleven rocks of AVIRIS (left) and MASTER (right).

Chapter 4. A Rule Based System for Integrating VNIR/SWIR and TIR data

Abstract

Previous research has shown that integrating hyperspectral VNIR/SWIR with multispectral TIR data can lead to improved mineral and rock identification. However, inconsistent results were found regarding the relative accuracies of different classification methods for dealing with the integrated data set.

In this study, a rule based system was developed for integration of VNIR/SWIR hyperspectral data with TIR multispectral data, and evaluated with a case study of Cuprite, Nevada. Previous geological mapping (Abrams and Ashley, 1980), supplemented by field work and sample spectral measurements, was used to develop a generalized knowledge base for analysis of both spectral reflectance and spectral emissivity. The characteristic absorption features, albedo, and the location of the spectral emissivity minimum were used to construct the decision rules. A continuum removal algorithm was used to identify absorption features from VNIR/SWIR hyperspectral data only; spectral angle mapper (SAM) and spectral feature fitting (SFF) algorithms were used to estimate the most likely rock type. The rule based system was found to achieve a notably higher performance than SAM, SFF, minimum distance, and maximum likelihood classification methods on their own.

Key Words: hyperspectral; multispectral; visible; near infrared; short wave infrared; thermal; classification methods; data integration; rule based system.

1. Introduction

Hyperspectral sensors, sometimes called imaging spectrometers, measure reflected solar energy in many narrow, contiguous bands from the visible and near infrared (VNIR) to the short wave infrared (SWIR), typically from 0.4 to 2.5 μm. Imaging spectroscopy has shown great potential for mapping minerals and rock composites because the narrow bands resolve the diagnostic absorption features associated with specific chemical bonds and physical structure of minerals and rocks (Farmer, 1974; Hunt, 1977, 1982; Clark, *et al*., 1990; Clark, 1999). Hyperspectral imagery has been used in geological investigations for over two decades, and during that time a wide range of data processing routines and spectral analysis algorithms have been developed (Boardman, 1989; Boardman *et al.,* 1995; Clark *et al.,* 1990, 1995; Gao *et al*., 1991; Green, 1990; Green *et al*., 1993; Kruse *et al*., 1993a; Kruse *et al*.1993b; Leprieur *et al.,* 1995; Roberts *et al.*, 1997; Staenz *et al.*, 1996; Van der Meer and Bakker, 1997).

One approach that has been successfully used for mineralogical and lithological mapping is that of an expert system (Kruse *et al*., 1993b; Clark *et al*., 2003). Expert systems use decision rules derived from knowledge of the spectral or other properties of the classes of interest. A particular advantage of expert systems is that they can exploit information selectively from the full range of information embedded in each pixel's spectrum.

The USGS Tetracorder Expert System, one of the most well known hyperspectral expert system for mineralogical mapping, contains data on more than 400 minerals, vegetation species, snow cover types, and manmade materials (Clark *et al*., 1990, 2003; Clark and Swayze, 1995). It utilizes two basic algorithms: a continuum removal

algorithm to extract absorption features, and a least-squares algorithm to calculate the goodness of fit between library reference spectra and remotely sensed spectra. The Tetracorder Expert System identifies surface materials by identifying one or more diagnostic absorption features, and has achieved good results even for minerals with relatively similar absorption features (Dalton *et al.,* 2004).

Spectral analysis methods that focus on absorption features are, however, less successful in identifying minerals having only limited or no diagnostic absorption features. For example, the silicate mineral quartz, which dominates many crustal rocks, does not exhibit any diagnostic absorption feature in the VNIR/SWIR region, although it does have spectral features in the thermal infrared (TIR) wavelength region (8-14 μm).

The example of quartz, given above, suggests that information complementary to that obtained in VNIR/SWIR wavelengths can potentially be obtained from the TIR wavelength region. Indeed, silicate minerals in general have TIR diagnostic features related to the characteristics of their silicon-oxygen bonds. Thus, most studies using multispectral TIR data for lithological mapping have focused on silicate or silicate-bearing rocks (Abrams *et al*., 1991; Gillespie *et al*., 1984; Hook *et al*., 1992, 1994, 1998; Lahren *et al*., 1988; Rowan, 1998; Sabine *et al*., 1994). Despite the advantages of using TIR, it is important to note that lithological mapping using multispectral TIR data is limited by the small number and broad wavelength intervals covered by the multispectral bands. In addition, the presence of weathering materials, desert varnish, and vegetation dilute the spectral features.

The combination of VNIR/SWIR hyperspectral data and multispectral TIR data can potentially be an effective combination for lithologic mapping (Abrams and Hook,

1991; Chen *et al.,* 2004, 2005). However, in experiments with simulated (Chapter 2) and real data (Chapter 3), the standard hyperspectral analysis approaches of spectral angle mapper (SAM) and spectral feature fitting (SFF) show some problems when applied to combined VNIR/SWIR/TIR data sets. SFF was found to take advantage of strong distinctive absorption features in the spectra, but it resulted in relatively poor performance when applied to rocks with low albedo and with no diagnostic absorption features, particular in the TIR region. By comparison, SAM achieved better results in discriminating low albedo volcanic rocks, but was not as good as SFF for rocks with strong diagnostic absorption features.

Based on observations in these previous chapters that different minerals were found to be most effectively classified using different wavelength regions and different methods (Chen *et al.,* 2004, 2005), a rule based system algorithm was developed for this paper to integrate hyperspectral VNIR/SWIR and multispectral TIR data. The rule based system was designed to draw on the strengths of SFF and SAM, as well as to exploit the spectral information selectively from the full range of VNIR, SWIR, and TIR wavelengths. The rule based system developed in this research was evaluated using a case study of Cuprite, Nevada, a well known test site for geological application using remote sensing techniques (Abrams *et al*., 1977a; Abrams *et al*., 1977b; Abrams and Ashley, 1980; Goetz and Srivastava, 1985; Abrams and Hook, 1991; Kruse *et al*., 1990; Hook *et al*., 1992; Van der Meer and Bakker, 1997). The study area is described in more detail in the next section.

2. Geological setting of study area

Cuprite is an ideal choice for testing mineral and rock classification methods because a wide range of volcanic, sedimentary, igneous, and metamorphic rocks, as well as hydrothermal alteration types, are exposed in a sparsely vegetated environment. In addition, a wide range of data sets is available for the site.

Cuprite is located in southwest Nevada (37° 29′ to 37° 35′ North, 117° 9′ to 117° 17′ West), near the California border. The oldest rock units, Cambrian siltstone, sandstone and limestone, dominate in the western part of the study area (Abrams and Ashley, 1980). Dominating the northeast of the area are two uppermost Tertiary volcanic rock units, which are comprised of sanidine-bearing sodic peralkaline rhyolite ash-flow tuffs. Porphyritic plagioclase-olivine basalt flows are exposed at several places. A number of large felsite dikes containing feldspar and scarce biotite phenocryts were intruded along north-trending faults in the southwest of the study area.

Most of the Tertiary volcanic rocks were to varying degrees hydrothermally altered in middle to late-Miocene times, creating fossilized hot-spring deposits (Buchanan *et al.,* 1981). The alteration has been divided into three zones based on alteration intensity: silicified, opalized, and argillized (Ashley and Abrams, 1980). The alteration zones in eastern study area form a bull's eye pattern, with the silicified zone at the core, surrounded by opalized, then argillized zones, which border the unaltered country rocks.

The silicified rocks are the most intensively altered, and the relict textures of the original rocks no longer exit. Silificied rocks comprise abundant quartz, some calcite, and minor alunite and kaolinite. About 10-30 percent desert vanish is present on the

weathering surface of the silicified rocks. The opalized rocks, forming the most widespread alteration, contain opal and abundant alunite and kaolinite. Primary quartz phenocrysts are occasionally present as relict minerals. The argillized rocks, which are the least intensively altered, are usually located within opalized zones or at the edge of the altered areas. Glass of the original volcanic rocks is altered to opal, montmorillonite, and kaolinite, and plagioclase is altered to kaolinite; primary quartz and sanidine are unaltered. Small amount of hematite may be present in argillized and opalized rocks (Abrams *et al.,* 1977a, 1977b; Abrams and Ashley, 1980).

3. Data sets of study area and preprocessing

There is no current sensor that simultaneously acquires hyperspectral VNIR/SWIR data and multispectral TIR data. Therefore, two separate data sets were obtained, and co-registered, as described below.

3.1 AVIRIS data

The hyperspectral VNIR/SWIR data were acquired by the Airborne Visible/Infrared Imaging Spectrometer (AVIRIS) (Green *et al.,* 1998) flown aboard the NASA ER-2 aircraft at a 20 km altitude on June 19, 1996, under cloud free weather conditions (Figure 4.1, left). AVIRIS has 224 contiguous bands at approximately 10 nm intervals between 0.4 and 2.5 μm. The AVIRIS instrument has an instantaneous field of view (IFOV) of 1 mrad, producing pixels of approximately 20 m, and a swath width of about 10 km. A single flight line covers whole study area. The radiometric calibration to reflectance was carried out by NASA Jet Propulsion Laboratory (JPL).

3.2 MASTER data

The multispectral TIR data was collected by the MODIS/ASTER Airborne Simulator (MASTER) (Hook *et al.,* 2001) at approximately 19:36 GMT on June 9, 1999, under clear weather conditions (Figure 4.1, right). The sensor was flown on a US Department of Energy King Air B-200, at an altitude of approximately 8,000 meters above the ground. The MASTER instrument has an IFOV of 2.5 mrad, thus producing pixels of approximately 20 meters for this data set. Although MASTER acquires 50 bands of data in the 0.4 – 13 μm region, only the 10 TIR bands (8-13 μm) were used for this study, in order to complement the AVIRIS VNIR/SWIR bands.

3.3 Image preprocessing

The TIR radiance measured by MASTER has three components: ground radiance, reflected downwelling atmospheric radiance, and upwelling atmospheric radiance. The three radiance components are attenuated by atmospheric transmittance. The MODTRAN4 atmospheric model (Berk *et al.*, 1999) was used to estimate atmospheric transmittance, and both upwelling and downwelling atmospheric radiance. A local atmospheric profile, measured with a radiosonde at the time of over-flight, was used to initialize the atmospheric model. After atmospheric correction, the ground radiance is dependent on both emissivity and temperature, as defined by the Planck function.

The separation of temperature and emissivity is an underdetermined problem because there is always one more unknown than the number of radiance measurements for each pixel (Hook, *et al*., 1992). We used the alpha residual approach (Hook *et al.,*

1992), which results in alpha residual spectra that have a similar shape to emissivity spectra.

Both AVIRIS reflectance data and MASTER alpha residual data were rectified and coregistered using United States Geological Survey (USGS) standard black and white Digital Orthophoto Quarter Quadrangles (DOQQs), with 1 meter pixels, as a reference map. For the AVIRIS data, 92 ground control points (GCPs) were used to construct a second-order polynomial transformation equation. The transformed AVIRIS data has a root mean square (RMS) error of 0.72 pixels. The MASTER data has a more complex geometry, partly because it was acquired at a lower altitude than the AVIRIS data. Consequently a rubber sheeting transformation with 239 GCPs was used to rectify the MASTER data, with a RMS error of 0.89 pixels, based on 30 evaluation points. Both images were resampled to the same UTM grid, using a nearest neighbor approach.

4. Rule based system

The main objective of this research is the development of a rule based system for automated identification of minerals and rocks based on their characteristic spectral features in the VNIR/SWIR and TIR regions. The knowledge base for the analysis of reflective and emissivity spectra was derived from selected image spectra (Figure 4.2), supplemented by measured field spectra (Figure 4.3), and spectral libraries created by the Jet Propulsion Laboratory (Grove *et al*., 1992), the U. S. Geological Survey (Clark *et al*., 1993), and Johns Hopkins University (Salisbury *et al.,* 1991; Research Systems, 2002). In addition, previous work on classifying simulated (Chapter 2, Chen et al. 2004) and real (Chapter 3, Chen *et al.,* 2005) data sets was important in identifying the optimal method for classifying each mineral.

4.1 Reflectance spectra and emissivity spectra analysis

The knowledge base for the rule based system was developed from analyses of rock spectra in both VNIR/SWIR and TIR regions. The decision rules were constructed based on spectral characteristics of rocks, including albedo, absorption features in VNIR/SWIR region, and spectral features in TIR region. (Table 4.1). These spectral characteristics were related to electronic or vibrational processes resulting from the interaction of electromagnetic energy with the atoms and molecules which compose the minerals that make up a rock. Iron dioxide, hydroxyl, and carbonate minerals exhibit absorption features in VNIR/SWIR region. By contrast, most silicate minerals have spectral features in TIR region (Lyon, 1972; Hunt, 1980).

Rock types of interest in this study include volcanic tuffs, basalt, diabase, felsite, limestone, siltstone, and sandstone, as well as the three alteration types of argillized, opalized, and silicified. Rock samples were collected in the field for subsequent laboratory spectral analysis.

A laboratory Fourier Transform Infrared (FTIR) spectrophotometer was used to acquire spectra over the range from 2.0–14.0 μm. The reflectance measurements then were converted to emissivity spectra using Kirchhoff's law. For VNIR/SWIR spectra, a FieldSpec Pro Full Range (0.4–2.5 μm) (Analytical Spectral Devices, Boulder, Colorado) field portable spectrometer was used. Both reflectance and emissivity spectra were resampled to AVIRIS and MASTER band passes respectively (Figure 4.3).

These reflectance spectra (0.4-2.5 μm) and emissivity spectra (8-13 μm) exhibit distinctive spectral features that can be related to rock composition (Table 4.1). Silicified rocks exhibit a relative weak absorption feature centered near 2.3 μm, but a distinctive

emittance low at 9.0 μm, due to quartz. Opalized rocks exhibit strong diagnostic features at 1.5, 1.8, 2.2, and 2.3 μm which are related to alunite and kaolinite absorption features. Argillized rocks contain montmorillonite, kaolinite, and small amount of hematite. Therefore they show characteristic absorption features centered near 2.2 μm due to clay minerals, and centered near 0.5 and 0.9 μm related to hematite-absorption. Opalized and argillized rocks also have broad emittance minima in the TIR region, but they are not distinctive. All volcanic rocks, including ash-flow tuffs, basalt, and diabase, have a low albedo, with a maximum reflectance less than 0.4. These silicate-bearing rocks show relative flat spectra without diagnostic absorption features in VNIR/SWIR region. However they exhibit an emittance minimum in the region 9.0-9.7 μm due to the presence of a Si-O bond. Limestone exhibits a diagnostic absorption feature related to carbonate feature at 2.3 μm and a weak spectral feature at 11.3 μm. The other quartz-bearing rocks, such as sandstone, also show a diagnostic emittance low at 9.0 μm. Siltstone exhibits absorption features located at 2.2, and 2.3, as well as an emittance low at 9.7 μm. In addition to the quartz-feature, sandstone exhibits an absorption feature at 2.2 μm. Felsite rocks show the silicate emittance low near 9.0-9.7 μm. The latter feature is not as distinctive as the 2.2 μm absorption feature.

4.2 Spectral feature matching algorithms

The rule based system developed in this study generally treats the reflective solar and TIR regions separately. Many diagnostic absorption features of minerals are potentially isolated in the hyperspectral AVIRIS data because the spectral width of absorption features ranges can be as narrow as 20 nm to 40 nm in the NIR and SWIR

wavelength region. As discussed above, the MASTER data, however, has only 10 bands in TIR wavelength region (8-13 μm), and these are relatively broad bands. Most narrow absorption features are not evident in the multispectral TIR data, and only the shape of spectra and the broad absorption features are distinguishable.

In Chapters 2 and 3 it was found that SAM and SFF algorithms have varying effectiveness for identifying different minerals and rocks using different wavelength regions (Table 4.2). SAM show some advantages over SFF in identifying minerals and rocks with low albedo and relative flat spectral features. On other hand, SFF achieves better performance when it deals with minerals and rocks exhibiting strong diagnostic absorption features. Therefore, the rule based system employs different spectral feature matching algorithms depending on the nature of the input spectrum.

For AVIRIS data, if the observed spectrum exhibits characteristic absorption features, the processing follows the SFF procedure used in the USGS Tetracorder System (Clark *et al*., 2003). Reflective absorption features are extracted using the continuum removal approach to suppress the effects of pixel mixtures. A least-square fit is calculated to compare each diagnostic absorption feature in the pixel spectrum to the continuum-removed reference spectra. The solution is obtained using the standard linear least-square algorithm defined as follows:

$$b = \frac{\sum_{c=1}^{n}(O_c L_c) - \frac{\sum_{c=1}^{n} O_c \sum_{c=1}^{n} L_c}{n}}{\sum_{c=1}^{n} L_c^2 - \frac{(\sum_{c=1}^{n} L_c)^2}{n}} \qquad (1)$$

$$b` = \frac{\sum_{c=1}^{n}(O_c L_c) - \frac{\sum_{c=1}^{n} O_c \sum_{c=1}^{n} L_c}{n}}{\sum_{c=1}^{n} O_c^2 - \frac{(\sum_{c=1}^{n} O_c)^2}{n}} \qquad (2)$$

$$F = (bb`)^{1/2} \qquad (3)$$

Where

O_c = the continuum removed pixel spectrum;

L_c = the continuum removed reference spectrum;

n = the number of bands covered by the absorption feature;

c = the band number;

F = the correlation coefficient;

If a material in the spectral library has multiple absorption features, a weighted fit is calculated separately for each feature in the reference spectrum, and then the results are combined (Clark *et al*., 2003). The weight value is signed empirically based on its depth, width, and significance. If the observed spectrum does not show any strong characteristic absorption features, SAM is used to estimate the spectral feature matching. SAM calculates the angle between the vector of observed pixel spectrum and vectors of reference spectra, and assigns the pixel with the reference class having smallest angle (Kruse *et al*., 1993a). In this study, the cosine of the angle is calculated instead of the angle itself. Therefore, the pixel is assigned with the reference class having the largest value.

For the multispectral TIR MASTER data, the spectral feature matching is carried out using original spectra, instead of the continuum removed spectra used for the AVIRIS

data, because the overall spectral shape of the TIR data may contain useful information for identifying minerals and rocks. Two methods are used to identify rocks depending on their spectral features. For pixels showing strong emittance features, such as the quartz-feature, the wavelength of the minimum emittance is determined using a least-squares fit approach similar to that used for the AVIRIS data is used. Otherwise, the observed spectrum is compared to the reference spectra using the SAM algorithm.

All spectral signatures of rocks were derived from the averaged pixel spectra based on the relative homogeneous area corresponding to geological map (Abrams and Ashley, 1980) and field work.

4.3 Decision rules

The rule based system consists of a hierarchy of decision rules that associate input pixel spectra with a single rock type. The VNIR/SWIR albedo and the presence of diagnostic absorption features are used in the decision rules. In order to take advantage of the systematic shift of emissivity minima with different silicate bearing rocks (Lyon, 1972; Hunt, 1980), the position of minimum in the MASTER TIR spectrum is also identified. The rules assign each pixel to just one class, or if the pixel fails to reach a predetermined confidence threshold, it is assigned to the class Unknown. To simplify the rule based system, the confidence threshold is set empirically to 0.1 for SAM and 0.5 for SFF. The rule based system is designed to assign mixed classes to the dominant endmember. The decision to avoid multiple classes was chosen to keep the results relatively simple, and to facilitate the evaluation of the method by comparison of the results with the generalized geological map.

The decision tree hierarchy is illustrated in Figure 4.4. The first rule is to determine if the pixel belongs to the low albedo group of rocks or minerals by checking if the maximum reflectance is less than 0.4. For those pixels that are in the low albedo group, SAM is applied to the combined data set to differentiate between limestone, tuff1, tuff2, basalt, and diabase. The second rule is applied to high albedo pixels, and checks for clay absorption features in the 2.09-2.25 μm region using the reference spectrum of argillized rock and SFF. An empirical value of 0.9 was chosen as the threshold correlation for separating pixels having the clay absorption feature. Pixels that show clay absorption features are classified as argillized or opalized rock using SFF and AVIRIS data. The third decision rule is to check if the wavelength of emittance minimum is greater than 9.0 μm. Most silicified rock and sandstone pixels have an emittance minimum at 9.0 μm or less, and SFF applied to the combined data set is used to differentiate these two classes. Pixels that have an emittance minimum greater than 9.0 μm are also classified using SFF, except in this case only the AVIRIS data is used, and the candidate classes are siltstone and felsite.

4.4 Evaluation of the rule based system

The rule based system applied to the Cuprite, Nevada data (Figure 4.5 Right) was evaluated by comparing the results to the distribution of rock units shown in the generalized geological map of Abrams and Ashley (1980), supplemented by field work conducted in 2004. Unconsolidated deposits and unclassified pixels were assigned to a background class (zero).

5. Results and discussion

For the rule based system, the area classified as hydrothermal alteration generally agrees with the distributions of alteration zones on the geological map (Abrams and Ashley, 1980). In particular, the regions classified as silicified rock are consistent with the distribution on the geological map

The most conspicuous disagreement between alteration zones shown on the geological map and the rule based system is in the distribution of argillized zones on the west side of study area. In this region, the geological map indicates only a few places where argillized rocks are found. In contrast, the rule based system identified a broad area of argillized rocks. The transitional nature of the argillized zones makes this class difficult to differentiate, even in hand specimen, from the unaltered country rock and the more intensely altered opalized zone. Identification of argillized rock is mainly based on the clay absorption feature at 2.2 μm, and the hematite related absorption features at 0.5 and 0.9 μm. The pattern of argillized zones separating opalized zones and country rocks on the west side of study area appears reasonable. However, further field work is needed to verify this interpretation.

Most volcanic rocks are classified correctly, as indicated by the distribution of these rocks on the geological map (Abrams and Ashley, 1980). With the exception of felsite, most volcanic rocks have a low albedo, and no characteristic absorption features in the AVIRIS data. Thus the volcanic rocks are generally discriminated based on their overall shape in the VNIR/SWIR and their spectral feature in the TIR region. Felsite is identified based on a characteristic double absorption feature at 2.2 and 2.4 μm. Diabase

is not shown on the geological map, but the extent of diabase as indicated by the rule based system agrees well with the field mapping.

The limestone identified by the rule based system also agrees well with the distribution of limestone on the geological map. Limestone can be identified due to its weak distinctive absorption features at 2.2 and 11.3 μm. Sandstone and siltstone are not separated on the geological map, but are grouped into the lower Cambrian Harkless Formation (Abrams and Ashley, 1980). Sandstone can be identified in the imagery due to its absorption features at 2.2 and 9.0 μm, whereas siltstone has spectral features at 2.2, 2.3, and 9.7 μm. Confirmation of this separation also requires future additional field work.

By comparison with the other methods applied to AVIRIS, MASTER, and combined data, as discussed in Chapter 3, the rule based system applied to the combined data achieved the highest accuracy of the different approaches used. The overall accuracy of the classification with the rule based system is more than 90 percent, almost 4 percent higher than the second highest accuracy obtained with SAM. As mentioned above, SAM applied to the combined data is effective for discriminating rocks which have a low albedo, a relatively flat spectra in the VNIR/SWIR region, and a broad emittance low in the TIR. For example, the SAM accuracy is the highest for limestone, tuffs, basalt, and diabase, irrespective of the data set (AVIRIS, MASTER, or combined) (Table 4.2). SFF is effective in identifying rocks with strong absorption features. Opalized rocks, argillized rocks, and felsite exhibit multiple characteristic absorption features in the VNIR/SWIR region. Thus, SFF applied to AVIRIS data obtained the highest accuracies for those rock units. SFF applied to the combined data also achieved

the highest accuracy for silicified rock and sandstone due to their characteristic absorption features in both the VNIR/SWIR and TIR regions. The classification accuracy of each individual rock (Table 4.3) shows that the rule based system successfully draws on the information in the AVIRIS and MASTER TIR data, using the optimum combination of SAM and SFF algorithms. The accuracies of most rock units are close to, or even better than, the highest accuracy of each individual rock unit with all methods and all data sets. The only exception is felsite, where some silicified rock pixels were mislabeled as felsite. The decision rule based on the wavelength position of the emissivity minimum was the source of some misclassification of silicified rocks.

6. Summary and conclusions

AVIRIS and MASTER data acquired over Cuprite, Nevada, on June 19, 1996 and June 9, 1999, respectively, were used to evaluate the integration of hyperspectral VNIR/SWIR with multispectral TIR data for geological mapping. The AVIRIS data were converted to estimated reflectance. The MASTER TIR data were corrected for atmospheric effects, and converted to emissivity with the alpha residual algorithm. A rule based system was developed that allows automated identification of rock units based on spectral features in the VNIR/SWIR and TIR regions. A set of decision rules was established based on analyzing spectra of field samples, as well as generic library spectra of selected common rock types and minerals in the study area. In addition to the characteristic absorption features of rocks, the albedo and the wavelength position of emissivity minimum was taken into consideration for defining the decision rules. SAM and SFF were employed to estimate the fitness of relative flat spectrum while SFF was used to calculate the match of the spectrum with strong spectral features.

The rule based system produced a classification map from AVIRIS and MASTER TIR data showing the predominant surface lithology. This classification map agreed with the previous geological map, and provides additional information about unmapped rock units. Several outcrops of diabase corresponding to Tertiary intrusives were identified with the rule based system, and verified in a field trip. More detailed information about lower Cambrian sedimentary rocks, specifically the potential discrimination of sandstone and siltstone, requires further field checking.

By comparison of the other classification methods, the rule based system was found to achieve a higher performance than SAM, SFF, minimum distance, and maximum likelihood classification methods on their own. The rule based system draws on the strengths of each of the two classification methods used, SAM and SFF. The rule based system demonstrates the value of acquiring simultaneous VNIR, SWIR, TIR imagery for geological mapping. It may serve as a model for future research in combining disparate wavelength data.

Acknowledgements

The authors would like to thank NASA Jet Propulsion Laboratory scientists Simon Hook and Ron Alley for providing us with an atmospheric profile acquired at the time of over-flight, and Cindy Grove for measuring the FTIR spectra of the field samples. Support for this research was provided by West Virginia View.

References

Abrams, M. J. and R. P. Ashley, 1980. Alteration mapping using multispectral images – Cuprite Mining District, Esmeralda County, Nevada. *U. S. Geological Survey Open File Report* 80-367.

Abrams, M. J., R. P. Ashley, L. C. Rowan, A. F. H. Goetz, and A. B. Kahle, 1977a. Use of imaging in the 0.46-2.36 μm spectral region for alteration mapping in the Cuprite mining district, Nevada. *U. S. Geological Survey Open-File Report* 77-585, pp.18.

Abrams, M. J., R. P. Ashley, L. C. Rowan, A. F. H. Goetz, and A. B. Kahle, 1977b. Mapping of hydrothermal alteration in the Cuprite mining district, Nevada, using aircraft scanner imagery for the 0.46-2.36 μm spectral region. *Geology* 5:713-718.

Abrams, M. J. and S. J. Hook, 1991. Combined use of TIMS and AVIRIS for alteration mapping: In *Proceedings of the third Thermal Infrared Multispectral Scanner (TIMS) Workshop*, JPL Publication 91-29, 54-64.

Abrams, M. J., E. A. Abbott, and A. B. Kahle, 1991. Combined use of visible, reflected infrared and thermal infrared images for mapping Hawaiian lava flow. *Journal of Geophysical Research*, 96: 475-484.

Boardman, J. W., 1989. Inversion of imaging spectrometry data using singular value decomposition. *Proceedings, IGARSS'89, 12th Canadian Symposium on Remote Sensing*, 4:2069-2070.

Boardman, J. W., F. A. Kruse, and R. O. Green, 1995. Mapping target signatures via partial unmixing of AVIRIS data. *Summaries, Fifth JPL Airborne Earth Science Workshop*, JPL Publication 95-1, 1:23-26.

Chen, X., Warner, T. A., and Campagna, D. J., 2004. Integrating visible, near infrared and short wave infrared hyperspectral and multispectral thermal imagery for geologic mapping: Simulated data, in: *Proceedings of 2004 AVIRIS Workshop***,** JPL, Pasadena, CA, March 31 – April 2, 2004.

Chen, X., Warner, T. A., and Campagna, D. J., 2005. Integrating visible, near infrared and short wave infrared hyperspectral and multispectral thermal imagery for geologic mapping at Cuprite, Nevada. In *2005 Appalachian Remote Sensing Conference and Workshops*, May 10 -11, 2005.

Clark, R. N., A. J. Gallagher, and G. A. Swayze, 1990. Materials absorption band shape least-squares fit with library reference spectra. In *Proceedings of the Second Airborne Visible/Infrared Imaging Spectrometer (AVIRIS) Workshop*, JPL Publ. 90-54, Jet Propulsion Laboratory, Pasadena, CA, pp. 176-186.

Clark, R. N., G. A. Swayze, A. J, Gallagher, T. V. V. King, and W. M. Calvin, 1993. The U. S. Geological Survey, Digital Spectral Library: Version 1: 0.2 to 3.0 microns, *U. S. Geological Survey Open File Report* 93-592, pp. 1340.

Clark, R. N. and Swayze, G. A., 1995. Automated spectral analysis: Mapping minerals, amorphous materials , environmental materials, vegetation, water, ice and snow,

and other materials: The USGS Tricorder Algorithm. *Lunar and Planetary Science*, XXVI, 255-256.

Clark, R. N., 1999. Spectroscopy of rocks and minerals, and principles of spectroscopy. In: A. N. Rencz (Ed.), *Remote Sensing for the Earth Sciences: Manual of Remote Sensing,* 3 ed, Vol. 3, Chapter 1: 3-58, John Wiley and Sons, New York.

Clark, R. N., Swayze, G. A., Livo, K. E., Kokaly, R. F., Sutley, S. J., Dalton, J. B., McDougal, R. R., & Gent, C. A. (2003). Imaging Spectroscopy: earth and planetary remote sensing with the USGS Tetracorder and expert systems. *Journal of Geophysical research* 108 (E12), 5131, doi:10.1029/2002JE001847.

Dalton, J. B., D. J. Bove, C. S. Mladinich, and B. W. Rockwell, 2004. Identification of spectrally similar materials using the USGS Tetracorder algorithm: the calcite-epidote-chlorite problem. *Remote Sensing of Environment* 89: 455-466.

Farmer, V. C., ed., 1974. *The Infra-red Spectra of Minerals*. Mineralogical Society, London, 539 pp.

Gao, B. C., A. F. H. Goetz, and J. A. Zamudio, 1991. Removing atmospheric effects from AVIRIS data for surface reflectance retrievals. In *Proceedings of the Third Airborne Visible/Infrared Imaging Spectrometer (AVIRIS) Workshop*, JPL Publ. 91-28, Jet Propulsion Laboratory, Pasadena, CA, pp. 80-86.

Gillespie, A. R., A. B. Kahle, and F. D. Palluconi, 1984. Mapping alluvial fans in Death Valley, California, using multichannel thermal infrared images. *Geophysical Research Letter*, 11: 1153-1156.

Green, R. O., 1990. Retrieval of reflectance from calibrated radiance imagery measured by the airborne visible/infrared imaging spectrometer (AVIRIS) for lithological mapping of the Clark Mountain, California. In *Proceedings of the Second Airborne Visible/Infrared Imaging Spectrometer (AVIRIS) Workshop*, JPL Publ. 90-54, Jet Propulsion Laboratory, Pasadena, CA, pp. 167-175.

Green R. O., J. E. Conel, and D. A. Roberts, 1993. Estimation of aerosol optical depth and additional atmospheric parameters for the calculation of the reflectance from radiance measured by the Airborne Visible/Infrared Imaging Spectrometer. In *Summaries of the Fourth Annual JPL Airborne Geosciences Workshop*, JPL Publ. 93-26, Vol. 1, Jet Propulsion Laboratory, Pasadena, CA, pp. 73-76.

Green, R. O., M. L. Eastwood, C. M. Sarture, T. G. Chrien, M. Aronsson, B. J. Chippedale, J. A. Faust, B. E. Pavri, C. J. Chovit, M. Solis, M. R. Olah, and O. Williams, 1998. Imaging Spectroscopy and the Airborne Visible/Infrared Imaging Spectrometer (AVIRIS). *Remote Sensing of Environment* 65:227-248.

Grove, C. I., S. J. Hook, and E. D. Paylor, 1992. Laboratory reflectance spectra for 160 minerals 0.4-2.5 micrometers. *JPL Publication 92-2*, Jet Propulsion Laboratory, Pasadena, CA.

Hook, S. J., Gabell, A. R., Green, A. A., & Kealy, P. S. (1992). A comparison of techniques for extracting emissivity information from thermal infrared data for geologic studies. *Remote Sensing of Environment*, 42, 123-135.

Hook, S. J., Karlstrom, K. E., Miller, C. F., & McCaffrey, K. J. W. (1994). Mapping the Piute Mountains, California, with thermal infrared multispectral scanner (TIMS) images. *Journal of Geophysical Research*, 99, 15,605-15,622.

Hook, S. J., T. J. Cudahy, A. B. Kahle, and L. B. Whitbourn, 1998. Synergy of active and passive airborne thermal infrared systems for surface compositional mapping. *Journal of Geophysical Research*, 103: 18,269-18,276.

Hook, S. J., J. J. Myers, K. J. Thome, M. Fitzgerald, and A. B. Kahle, 2001. The MODIS/ASTER Airborne Simulator (MASTER) – a new instrument for earth science studies. *Remote Sensing of Environment* 76: 93-102.

Hunt, G. R., 1977. Spectral signatures of particulate minerals, in the visible and near infrared, *Geophysics*, 42: 501-513.

Hunt, G.R., 1980. Electromagnetic radiation: the communication link in remote sensing, in *Remote Sensing in Geology* (B.S. Siegal and A.R. Gillespie, Eds.). Wiley, New York, pp. 5-45.

Hunt, G. R., 1982. Spectroscopy properties of rocks and minerals, In R. S. Carmichael (Ed.), *Handbook of Physical Properties of Rocks*, Vol. 1, CRC Press, Boca Raton, Fla., pp. 295-385.

Hunt, G.R., and J. W. Salisbury, 1974. Mid-infrared spectral behavior of igneous rocks, In *Technical Report* AFRCL-TR-75-0356, US Air Force Cambridge Research Laboratory, Cambridge, MA.

Kruse, F. A., A. B. Lefkoff, J. B. Boardman, K. B. Heidebrecht, A. T. Shapiro, P. J. Barloon, and A. F. H. Goetz, 1993a. The spectral image processing system (SIPS) – Interactive visualization and analysis of imaging spectrometer data. *Remote Sensing of Environment* 44: 145-163.

Kruse, F. A., A. B. Lefkoff, and J. B. Dietz, 1993b. Expert system-based mineral mapping in Northern Death Valley, California/Nevada, Using the Airborne Visible/Infrared Imaging Spectrometer (AVIRIS). *Remote Sensing of Environment* 44: 309-336.

Lahren, M. M., R. A. Schweickert, and J. V. Taranik, 1988. Analysis of the northern Sierra accreted terrain, California, with airborne thermal infrared multispectral scanner data. *Geology*, 16: 525-528.

Leprieur, C., V. Carrere, and X. F. Gu, 1995. Atmospheric correction and ground reflectance recovery for airborne visible/infrared imaging spectrometer (AVIRIS) data, MAC Europe 91. *Photogrammetry Engineering and Remote Sensing* 61 (10): 1233-1238.

Lyon, R. J. P., 1972. Infrared spectral emittance in geologic mapping: Airborne spectrometer data from Pisgah Crater, CA. *Science* 175: 983-985.

Research Systems, 2004. *ENVI User's Guide, ENVI 3.6*. Research Systems, Boulder CO., pp. 1050.

Roberts, D. A., R. O. Green, and J. B. Adams, 1997. Temporal and spatial patterns in vegetation and atmospheric properties from AVIRIS. *Remote Sensing of Environment* 63 (3): 223-240.

Rowan, L. C., 1998. Analysis of simulated advanced spaceborne thermal emission and reflection (ASTER) radiometer data of the Iron Hill, Colorado, study area for mapping lithologies. *Journal of Geophysical Research D: Atmospheres* 103(24): 32,291-32,306.

Sabine, C., V.J. Realmuto, and J.V. Taranik, 1994. Quantitative estimation of granitoid composition from thermal infrared multispectral scanner (TIMS) data, Desolation Wilderness, northern Sierra Nevada, California. *Journal of Geophysical Research* 99(B3): 4261-4271.

Salisbury, J. W., L. S. Walter, N. Vergo, and D. M. D`Aria, 1991. Infrared (2.1-25 micrometers) Spectra of minerals. *Johns Hopkins University Press*, pp. 294.

Staenz, K., D. J. Williams, and B. Walker, 1996. Surface reflectance retrieval from AVIRIS data using a six dimensional look up table. In *Summaries of the sixth Annual JPL Airborne Earth Science Workshop*, Jet Propulsion Laboratory, Pasadena, CA, pp. 223-230.

Van der Meer, F. and W. Bakker, 1997. CCSM: Cross correlogram spectral matching. *International Journal of Remote Sensing* 18: 1197-1201.

Tables

Table 4.1. Spectral characteristics of selected rock types from Cuprite, Nevada

Rocks	Spectral Characteristics		
	Albedo	Spectral features	
		VNIR/SWIR	TIR
Silicified	High	2.3 μm	9.0 μm
Opalized	High	1.5, 1.8, 2.2, 2.3 μm	9.0 μm
Argillized	High	0.5, 0.9, 2.2 μm	9.7 μm
Tuff1	Low	N/A	9.7 μm
Tuff2	Low	N/A	9.7 μm
Basalt	Low	N/A	9.7 μm
Diabase	Low	N/A	9.0-9.7 μm
Limestone	Low	2.3 μm	11.3 μm
Siltstone	High	2.2, 2.3 μm	9.7 μm
Sandstone	High	2.2 μm	9.0 μm
Felsite	High	2.2, 2.4 μm	9.0-9.7 μm

Table 4.2. Classification accuracies of SAM and SFF applied to AVIRIS, MASTER, and combined data respectively (summarized from Chapter 3 & Chen *et al.*, 2005)

Rocks	Classification Accuracy (%)					
	SAM			SFF		
	AVIRIS	MASTER	Combined	AVIRIS	MASTER	Combined
Silicified	59.5	66.6	82.9	89.9	41.5	95.7
Opalized	77.7	43.8	78.0	82.4	34.0	70.1
Argillized	72.6	37.9	71.6	72.1	39.3	48.3
Tuff 1	76.4	56.2	95.3	68.9	63.7	67.8
Tuff 2	79.9	64.2	95.1	89.7	69.0	74.9
Basalt	51.5	78.7	93.0	46.9	79.9	83.1
Diabase	61.6	37.9	85.9	60.0	17.2	64.4
Limestone	80.3	92.4	99.8	97.6	74.0	92.6
Siltstone	91.1	89.7	91.6	88.7	87.1	89.4
Sandstone	91.2	59.9	90.5	81.5	43.3	92.2
Felsite	43.7	73.1	61.8	98.8	15.6	79.9
Overall accuracy	72.4	63.8	86.2	81.0	51.6	79.2

Table 4.3. Classification accuracies using the rule based system

Rocks	**Classification Accuracy (%)**		
	Producer's Accuracy	**User's Accuracy**	**Average Accuracy**
Silicified	87.5	98.7	93.1
Opalized	75.0	83.7	79.4
Argillized	75.7	67.0	71.4
Tuff1	99.2	86.8	93.0
Tuff2	93.8	95.6	94.7
Basalt	88.3	97.7	93.0
Diabase	91.4	91.8	91.6
Limestone	100.0	99.9	100.0
Siltstone	97.6	85.7	91.7
Sandstone	87.1	95.6	91.4
Felsite	92.6	95.0	88.8
Overall accuracy	90.1		

Figures

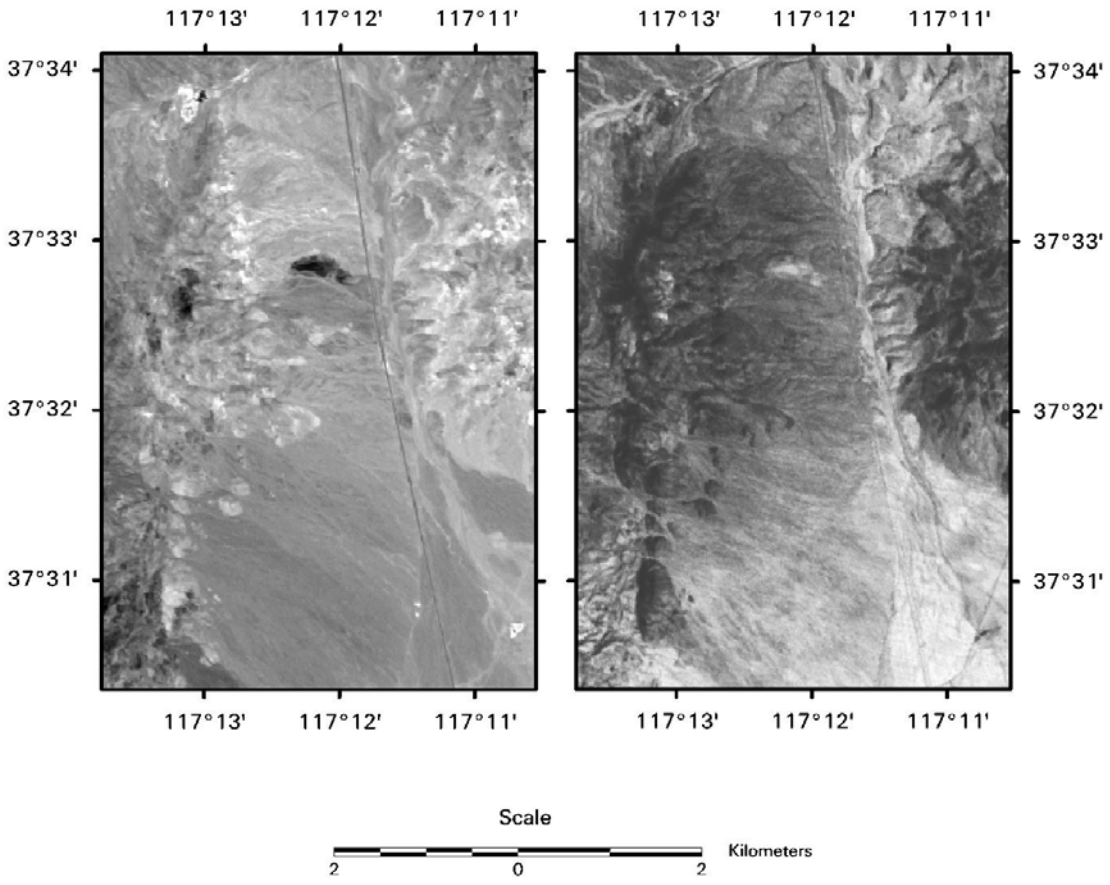

Figure 4.1 Left: AVIRIS image (band 199, 2.26 mm); Right: MASTER image (band 45, 9.67mm)

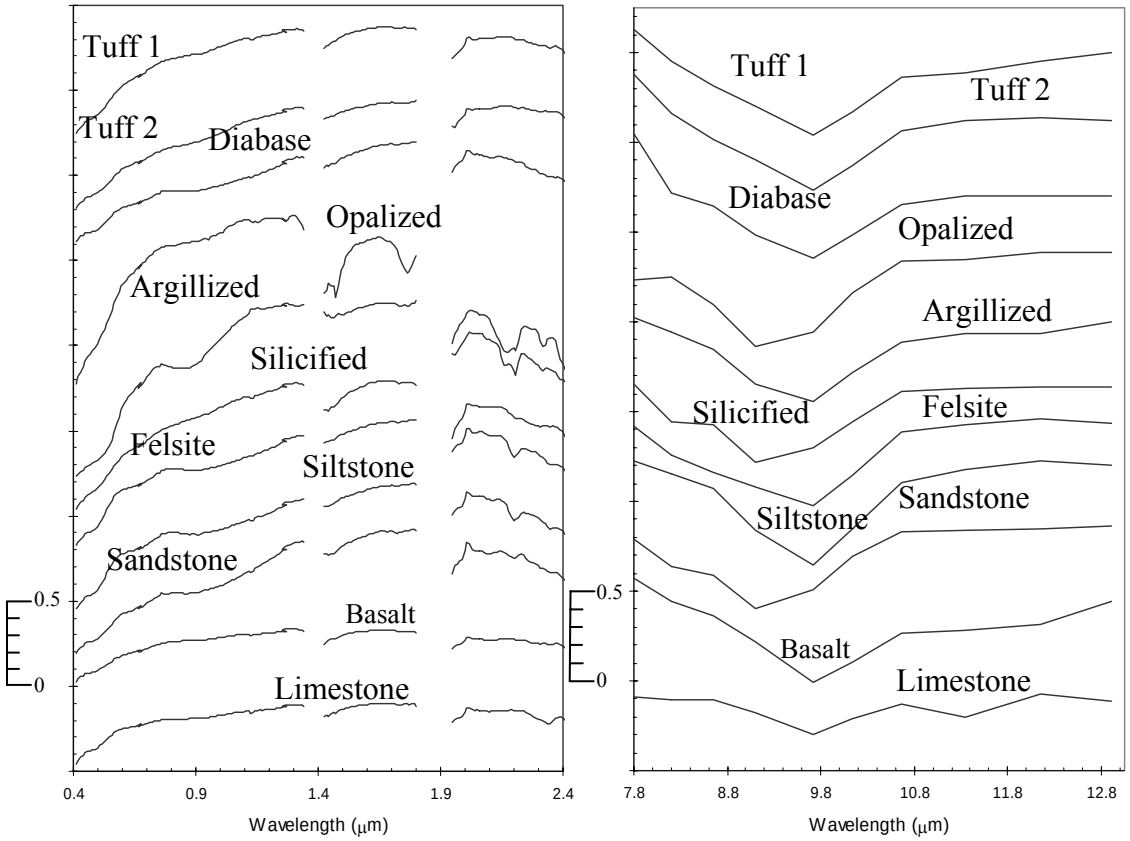

Figure 4.2. Image derived reflectance spectra and alpha emissivity residual spectra of eleven rocks of AVIRIS (left) and MASTER (right).

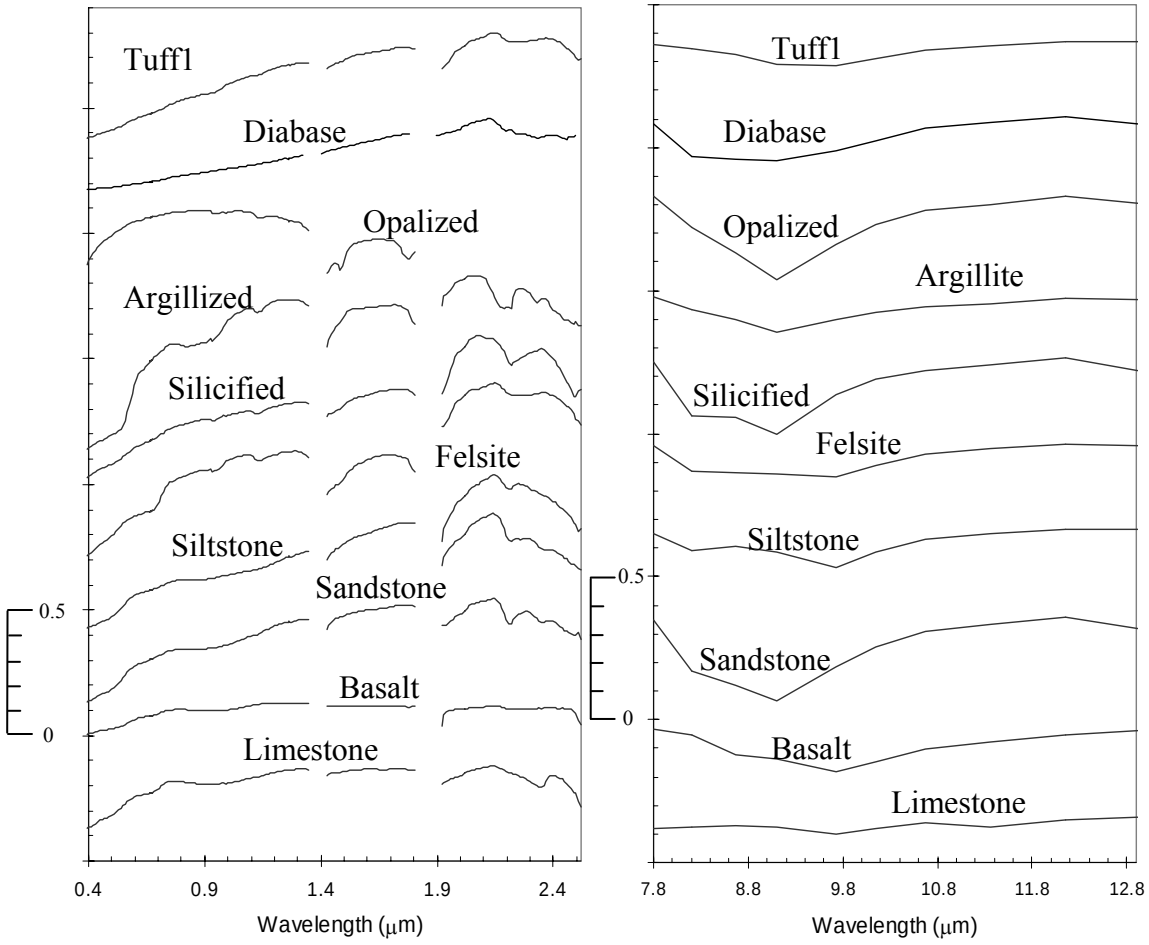

Figure 4.3. Measured reflectance spectra and alpha residual emissivity spectra of nine rocks resampled to AVIRIS (left) and MASTER (right) wavelength bands.

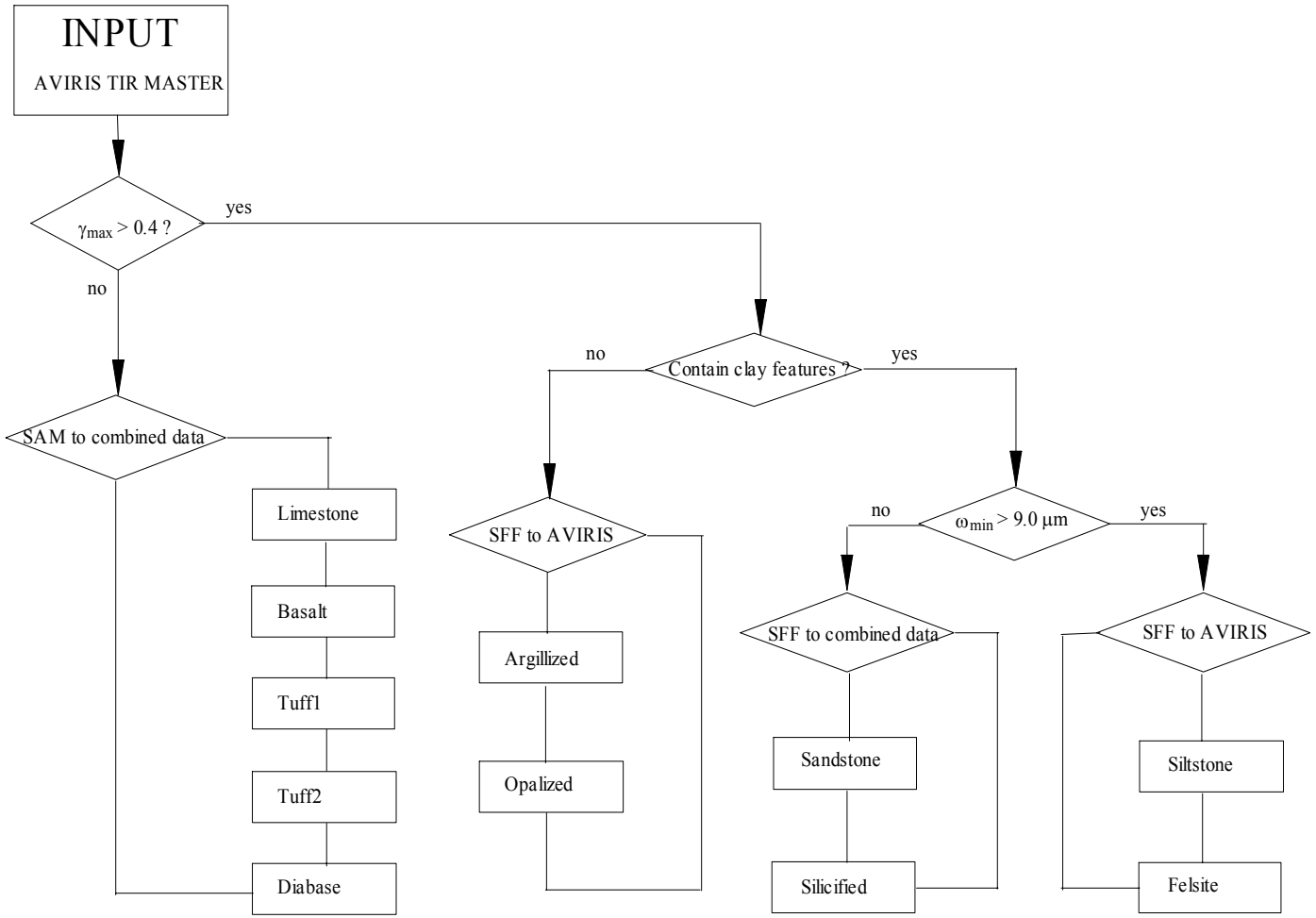

Figure 4.4 Flowchart of the rule based system. γ_{max} is maximum reflectance of pixel spectrum; ω_{min} is the wavelength of emissivity minima.

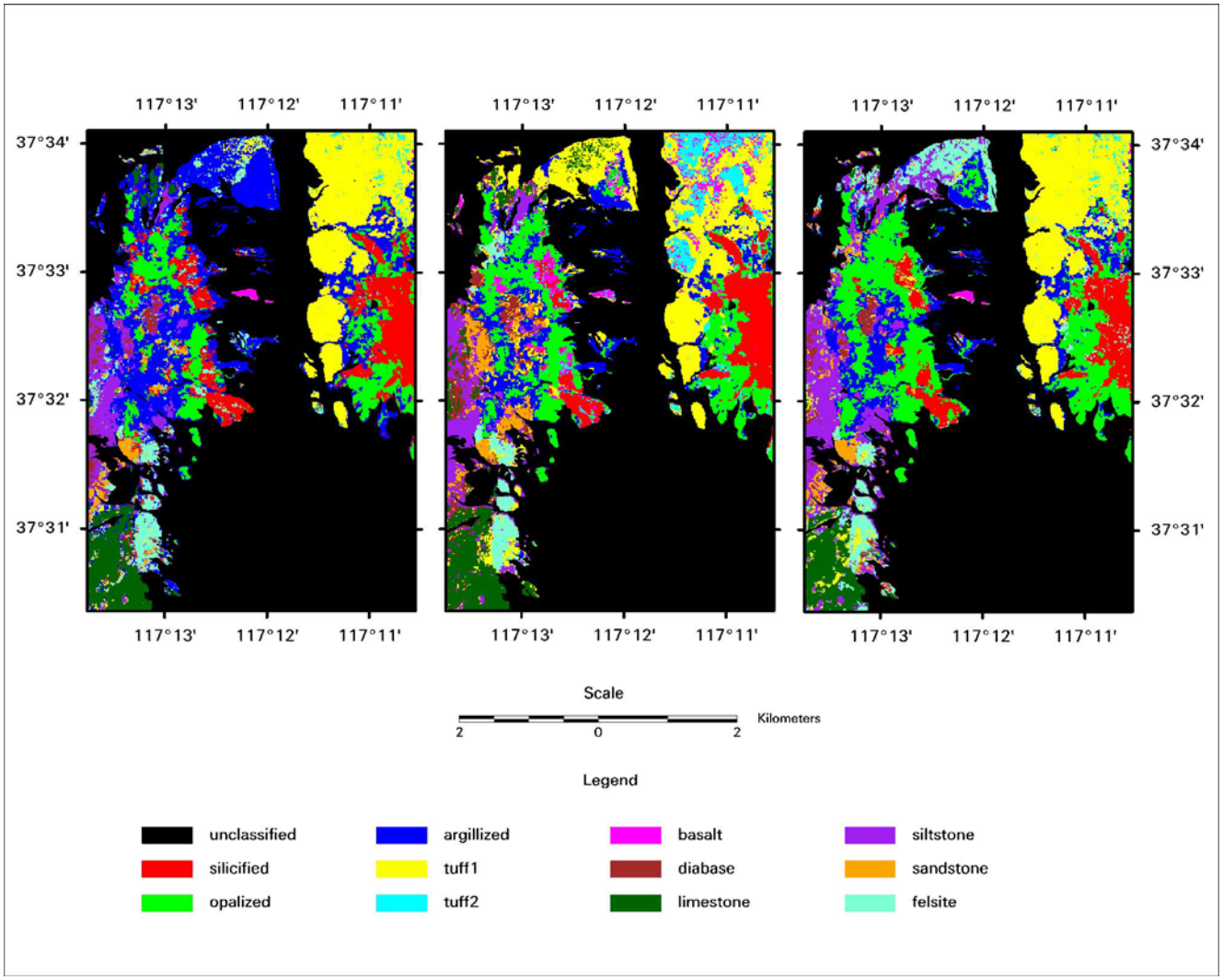

Figure 4.5. Classification results. Left: SAM applied to the combined data. Middle: SFF applied to AVIRIS data. Right: The rule based system.

Chapter 5. General Conclusions

This research investigated the potential of integrating VNIR/SWIR hyperspectral and TIR multispectral data for geological mapping. The simulated data analysis, real data analysis, and rule based system classification all clearly showed that the combination of these disparate data provided increased information.

The simulated data were developed from spectral library and sample measurements of rocks and minerals. Seven levels of uncertainty were identified and modeled. The simulated data provide a highly controlled data set, for which the true composition of each pixel is known. The real data experiments demonstrated the real world application of the simulated data work. The real data comprised AVIRIS and MASTER TIR imagery acquired over Cuprite, Nevada, a well known remote sensing test site. The rule based system was specifically designed to integrating these two disparate data types, and drew on the results of both the simulated and real data experiments. The rule based system selectively uses all or part of the combined pixel spectrum, and applied either SFF (Crowley *et al.,* 1989; Clark *et al.,* 1990) or SAM (Kruse *et al*., 1993) classification, depending on the spectral characteristics of each pixel.

The relative value of the combination of VNIR/SWIR and TIR data depends in part on the classification method used. For the simulated data analyses, most of the methods investigated, except binary encoding applied to the combined data, achieved improvements in overall classification accuracy in comparison to these methods used with the AVIRIS data set alone. For the real data analyses, SAM, minimum distance classification, and maximum likelihood classification showed improvement when used with the combined data set. However, SFF applied to the combination of AVIRIS and

TIR MASTER bands showed a decrease in classification accuracy. Thus, integrating these two wavelength regions only assisted discrimination of minerals and rocks which generally exhibit spectral features in the TIR region.

Part of the inconsistency between the different studies may arise from the effect of uncertainty. The simulated data analyses showed that most methods were sensitive to mixing uncertainty. The only exception is maximum likelihood classification, at least within the constraints of this study. SAM and SFF applied to the data set consisting of minerals exhibiting distinctive absorption features was found to be relative tolerant of mixing uncertainty. SAM, binary encoding, and SFF are less sensitive to illumination effects when they are applied to the simulated AVIRIS data sets. Maximum likelihood classification was found to be relatively robust in the presence of uncertainty, because in this study sufficient training samples were available to estimate the probability distribution accurately.

Evaluation of SAM, SFF, binary encoding, minimum distance, and maximum likelihood classification applied to simulated data indicated that maximum likelihood classification obtained the best performance, then followed by SAM and SFF; binary encoding and minimum distance classification had relative poor classification accuracies. However the real data analyses showed slightly different results. Applied to AVIRIS data, SFF obtained the highest classification accuracy, maximum likelihood classification took second place, followed by SAM; minimum distance classification had a relative low accuracy. On the other hand, with the combination of AVIRIS and TIR MASTER, SAM achieved the best performance, followed by minimum distance classification, SFF and maximum like likelihood classification. I interpret this to indicate that there were

insufficient training samples to estimate the covariance matrix of each class with sufficient reliability for maximum likelihood classification (Landgrebe, 2000). SAM and SFF do not use second order statistics, and therefore theoretically require fewer training samples.

SFF was generally superior to SAM in identification of minerals and rocks with distinctive absorption features, although the accuracy of SAM applied to the combined data sets was slightly better than that of SFF. SAM applied to the combined data sets increased classification accuracy for some minerals and rocks which do not exhibit distinct absorption feature in thermal infrared region, while for SFF, only the accuracy of minerals and rocks with characteristic absorption features in the thermal infrared region was improved. It was found that different methods had their own strength in dealing with specific wavelength regions and minerals and rocks. It was notable in the real data analysis that SAM applied to the combined data worked best for discriminating low albedo rock units. Most of the low albedo rocks are volcanics, which do not exhibit strong absorption features in the VNIR/SWIR regions, but have distinctive spectral features in the TIR. SFF applied to the AVIRIS data alone gave the best results for the opalized and argillized rocks, as well as siltstone and felsite, all of which have diagnostic absorption features in the VNIR/SWIR regions. SFF applied to the combined data was the best data and method combination for classifying silicified rock and sandstone, both of which have strong spectral features in the TIR.

The rule based system was developed to take advantages of spectral information across the spectrum from VNIR and SWIR, to TIR. The knowledge base was established from the image spectral analyses and by examining the library spectra and field sample

measurements. In addition to the characteristic absorption features of rocks, the albedo and the wavelength position of the emissivity minimum were used in defining the decision rules. Two spectral feature matching algorithms such as SAM and SFF were used for spectral matching based on spectral features in the TIR region. Therefore, the rule based system draws on the strength of the SAM and SFF algorithms. It achieved the highest accuracy of the various classification methods tested. The lithological map produced with the rule based system showed relatively strong agreement with distributions of these rocks on the geological map. Moreover, the resulting lithological map contained new information about the lithology of the study area not present on the map, including the presence of diabase.

The rule based system demonstrated the value of integrating VNIR, SWIR, and TIR imagery for geological mapping. It may serve as a model for future research in combining disparate wavelength data. These decision rules might be generalized in order to be useful in a wider range of areas. A generalized integrated classification method may particularly be relevant once Airborne Reflective Emissive Spectrometer (ARES) (Mueller *et al*., 2003) data are available., a new test site and new data can be used to test the rule based system.

References

Clark, R. N., Gallagher, A. J., & Swayze, G. A. (1990). Material absorption band depth mapping of imaging spectrometer data using the complete band shape least-squares algorithm simultaneously fit to multiple spectral features from multiple materials. *Proceedings of the Third Airborne Visible/Infrared Imaging Spectrometer (AVIRIS) Workshop*, JPL Publication 90-54, 176-186.

Crowley, J. K., Brickey, D. W., & Rowan, L. C. (1989). Airborne imaging spectrometer data of the Ruby Mountains, Montana: mineral discrimination using relative absorption band-depth images. *Remote Sensing of Environment*, 29, 121-134.

Kruse, F. A., Lefkoff, A. B., Boardman, J. B., Heidebrecht, K. B., Shapiro, A. T., Barloon, P. J., & Goetz, A. F. H. (1993a). The spectral image processing system (SIPS) – Interactive visualization and analysis of imaging spectrometer data. *Remote Sensing of Environment*, 44, 145-163.

Landgrebe, D. (2000). Information extraction principles and methods for multispectral and hyperspectral image data. In C. H. Chen (ed.), *Information Processing for Remote Sensing*, Chapter 1, NJ.: World Scientific Publishing Co., Inc., River Edge.

Mueller, Richter, A., R., Habermeyer, M., Mehl, H., Dech, S., Kaufmann, H., Segl, K., Haschberger, P., & Strobl, P. (2003). ARES: a new reflective/emissive imaging spectrometer for terrestrial application: In *Proceedings of thirteen Airborne Visible/Infrared Imaging Spectrometer (AVIRIS) and Hyperion Workshop*, Jet Propulsion Laboratory, Pasadena, California.